The Astronomical Journal, 132:378–392, 2006 July

THE RECENT STAR FORMATION IN NGC 6822 FROM *HUBBLE SPACE TELESCOPE* IMAGING[1]

Luciana Bianchi[2] and Boryana V. Efremova[2,3]

Received 2005 November 22; accepted 2006 March 30

ABSTRACT

We present *Hubble Space Telescope* WFPC2 and STIS imaging of the low-metallicity galaxy NGC 6822, performed as part of a study of the young stellar populations in the galaxies of the Local Group. Eleven WFPC2 pointings, with some overlap, cover two regions extending over 19 and 13 arcmin^2, respectively, off the galaxy center. The filters used are F170W, F255W, F336W, F439W, and F555W. One $25'' \times 25''$ field observed with the STIS FUV- and NUV-MAMA includes Hodge's OB 8 association and the H II region Hubble V, contained in field 1 of Bianchi et al.; this previous study provides additional WFPC2 four-band photometry. We derive the physical parameters of the stars in the fields and the extinction by comparing the photometry to grids of model magnitudes. The environments studied in this work include one of the most luminous (in Hα) H II regions in the Local Group (Hubble V) with a compact star cluster, a typical OB association (OB 15), the sparse field population, and the outskirts of NGC 6822. In the WFPC2 fields, most of the hot massive stars are found in the Hodge OB 15 association, at about 5′ (0.7 kpc) east of the galaxy center, extending $\approx$90″ ($\approx$200 pc) in our imaging. The color-magnitude diagram indicates a young age, $\leq$10 Myr, for this association, where we measure 70 stars hotter than $\sim$16,000 K (earlier than mid-B spectral type) according to their photometric colors. In the compact H II region Hubble V, we measure 80 stars brighter than $m_{\rm NUV} < 22.5$ mag and find most of them to have high temperatures. The density (per unit area) of hot massive stars in the core of the OB 8 association is higher than in OB 15 by a factor of 12, while the total stellar mass formed is similar ($\approx$4 or 7×10^3 $M_\odot$, when extrapolated to a mass range of 1–100 or 0.1–100 $M_\odot$, respectively). In both OB 15 and OB 8 massive star candidates are found. In the general field outside of the OB 15 association, we find few hot massive stars (0.7 arcmin^{-2}) and several A-type supergiants. No massive star candidates are found in the WFPC2 fields outside the main galaxy body ($\approx$10.′5–14.′5 [1.5–2 kpc] from the galaxy center), where the population is dominated by foreground stars, at least down to $V \sim 22$. At fainter magnitudes, we measure in these outer fields a significantly larger number of stars than the model for Milky Way foreground objects would predict. The average extinction is found to vary among the three environments studied: $E(B-V) = 0.22$ in the outer regions, $E(B-V) = 0.27$ in the fields east of the galaxy main bar, and $E(B-V) = 0.40$ in the H II region Hubble V. A quantitative discussion of the applicability of the reddening-free-index method for photometric determination of stellar parameters is provided for the filters used in this work, based on our grids of stellar models.

Key words: galaxies: individual (NGC 6822) — galaxies: photometry — galaxies: stellar content — Local Group

Online material: machine-readable tables

1. INTRODUCTION

The massive star populations of nearby galaxies are a subject of great interest due to the impact that massive stars have on the galaxies' properties and evolution. Massive stars, in their short lifetime, drive the chemical and dynamical evolution of the parent galaxies and trace the star formation activity. The most luminous, most massive stars provide information on the initial mass function (IMF) and its properties. The study of the IMF in different environments gives us a way to determine its dependence on parameters such as metallicity and star formation rate. The galaxies of the Local Group provide an excellent opportunity to investigate the modalities of star formation through the resolved studies of their stellar populations, because they are close enough so that individual stars can be accurately measured, and all the stars are at approximately the same, known distance; thus, their absolute luminosity can be derived. With its high resolving power and wide range of filters including UV wavelengths, the *Hubble Space Telescope* (*HST*) is the most suitable instrument for studying young stellar populations in the Local Group galaxies. In a global context, studies of resolved local starbursts provide a key to understanding distant star-forming galaxies, for which only integrated properties can be measured. Resolved studies of the stellar content, extinction, and global parameters of nearby starburst regions in different environments provide a calibration to interpret integrated studies of unresolved starbursts in distant galaxies.

NGC 6822 is an irregular dwarf galaxy, a member of the Local Group. The angular size of the galaxy at optical wavelengths is $6' \times 11'$, and its distance is estimated to be 500 kpc (McGonegal et al. 1983).

The old and intermediate stellar populations of NGC 6822 have been studied by Gallart et al. (1996a) in a central $11.'2 \times 10.'4$ area, and by Wyder (2003) in four *HST* WFPC2 fields, from *V*- and *I*-band photometry. Both studies infer from the color-magnitude diagram that star formation began 12–15 Gyr ago or more recently, depending on the initial metallicity assumed, and proceeded more or less uniformly until about 600 Myr ago. The young stellar population of NGC 6822 and its recent star formation history have also been the subject of previous photometric studies. The first galaxy-wide photographic *UBV* photometry of NGC 6822 was published by Kayser (1967), followed by a photographic

[1] Based on observations made with the NASA/ESA *Hubble Space Telescope*, obtained at the Space Telescope Science Institute, which is operated by the Association of Universities for Research in Astronomy, Inc., under NASA contract NAS5-26555.

[2] Center for Astrophysical Sciences, Department of Physics and Astronomy, The Johns Hopkins University, 3400 North Charles Street, Baltimore, MD 21218; bianchi@pha.jhu.edu, boryana@pha.jhu.edu.

[3] Department of Astronomy, University of Sofia, 5 James Bourcheir Street, Sofia 1126, Bulgaria.

TABLE 1
THE *HST* DATA (PROGRAM GO-8675)

			Exposure Time in Each Filter (s)						
			STIS Imaging		WFPC2 Imaging				
Field (Data Set Root)	R.A. (J2000.0)	Decl. (J2000.0)	FUV-MAMA	NUV-MAMA	F170W	F255W	F336W	F439W	F555W
NGC6822-PARFIELD10 (u6641)	19 45 06.47	−14 47 05.8			2 × 300	3 × 400	...	...	...
					2 × 500	2 × 500	2 × 350	2 × 350	2 × 100
					2 × 700	...	...	...	...
NGC6822-PARFIELD20 (u6642)	19 44 46.07	−14 38 17.2			2 × 300	1 × 300	...	...	...
					2 × 500	2 × 400	2 × 350	2 × 350	2 × 100
					2 × 700	2 × 500	...	...	...
NGC6822-PARFIELD30 (u66430)	19 44 47.97	−14 38 13.2			...	...	2 × 260	2 × 260	2 × 100
NGC6822-PARFIELD31 (u66431)	19 45 12.62	−14 42 45.8			2 × 500	2 × 500	2 × 300	2 × 260	2 × 100
NGC6822-PARFIELD32 (u66432)	19 45 14.25	−14 42 36.9			2 × 500	2 × 500	2 × 300	2 × 260	2 × 100
NGC6822-PARFIELD33 (u66433)	19 44 40.29	−14 38 59.5			2 × 500	2 × 500	2 × 300	2 × 260	2 × 100
NGC6822-PARFIELD34 (u66434)	19 44 39.18	−14 39 14.1			2 × 400	2 × 350	...	...	...
NGC6822-PARFIELD35 (u66435)	19 45 12.71	−14 44 23.9			...	...	2 × 260	2 × 260	2 × 100
NGC6822-PARFIELD36 (u66436)	19 45 11.26	−14 45 30.2			2 × 500	2 × 500	2 × 300	2 × 260	2 × 100
NGC6822-PARFIELD37 (u66437)	19 44 37.87	−14 39 22.5			2 × 500	2 × 500	2 × 300	2 × 260	2 × 100
NGC6822-PARFIELD38 (u66438)	19 44 44.88	−14 38 22.1			2 × 500	2 × 500	2 × 300	2 × 260	2 × 100
NGC6822-HV-LBFLD1 (o6641)	19 44 52.20	−14 43 14.5	1320	600					
NGC6822-HV-LBFLD1B (o6642)	19 44 52.12	−14 43 15.0	1320	480					

NOTE.—Units of right ascension are hours, minutes, and seconds, and units of declination are degrees, arcminutes, and arcseconds.

and photoelectric study by Hodge (1977), who cataloged 16 OB associations. The ground-based photometric study by Massey et al. (1995) found that O-type stars are present in several of the OB associations but that NGC 6822 is relatively poor in very massive stars compared to M31, M33, and the Magellanic Clouds; the reddening varies from $E(B-V) = 0.26$ on the periphery to 0.45 near the central regions, with an average ratio $E(U-B)/E(B-V)$ of 0.74 ± 0.07. Bianchi et al. (2001b) presented ground-based *UBV* CCD photometry covering the whole body of the galaxy and *HST* WFPC2 four-band photometry in two regions containing very rich and crowded OB associations. They found populations younger than 10 Myr in four of the OB associations included in their study, and in particular very young stellar populations (a few megayears) in the star-forming H II regions Hubble V and Hubble X (Hubble 1925). The outer parts of the galaxy are much less studied. No young stellar population was found in the two outer regions of NGC 6822 analyzed by Hutchings et al. (1999).

The search for young stars in different galaxy environments presented in this paper covers larger regions than previous *HST* studies, with deeper exposures, and has the advantages of the *HST* wider wavelength coverage (extending to the UV) and higher spatial resolution compared to ground-based *UBV* data. The UV bands (WFPC2 F170W and F255W, and STIS FUV-MAMA and NUV-MAMA) in addition to the *U*, *B*, and *V* bands allow us to identify the most massive, luminous stars. In fact, due to their high effective temperatures, the earliest spectral types cannot be differentiated from optical colors (see, e.g., the discussion in Massey 1998a; L. Bianchi & A. Tolea 2006, in preparation).

The observations and data reduction are described in § 2, the photometry measurements and the characteristics of the stellar populations are presented in § 3, and the results are discussed in § 4 and summarized in § 5.

2. OBSERVATIONS AND DATA REDUCTION: PHOTOMETRY

HST imaging of different regions in NGC 6822 were obtained between 2000 June 16 and 2002 May 24 as part of the program GO-8675 (principal investigator L. Bianchi) to study the massive star content of this galaxy, with the WFPC2 and the STIS imagers. The WFPC2 images were taken in parallel mode. We discuss the reduction and analysis procedures separately for the two sets of data.

2.1. *WFPC2 Imaging*

A total of 110 images in 11 different fields were obtained with WFPC2 on board *HST*. The instrument consists of four 800 × 800 CCD chips with angular resolution of 0.″046 pixel^{-1} (0.11 pc at the distance of 500 kpc to NGC 6822) for the Planetary Camera (PC) and 0.″099 pixel^{-1} (0.24 pc) for the Wide Field chips (WF2, WF3, and WF4). In most of the fields imaging was taken with five WFPC2 broadband filters: F170W, F255W, F336W, F439W, and F555W. Table 1 lists the field positions, the filters used, and the corresponding exposure times. The fields are partially overlapping and are grouped in two areas, east and northwest of the main body of the galaxy. The east group (group 1) covers about 19 arcmin^2 (≈402 kpc^2), and the northwest group (group 2) covers about 13 arcmin^2 (≈275 kpc^2). The positions of the fields are shown in Figure 1.

The images, which were processed with the Post Observation Data Processing System pipeline for bias removal and flatfielding, were downloaded from the MAST archive. In order to reject cosmic rays, images taken with the same pointing and filter were combined using the IRAF task CRREJ. This task combines multiple exposures at the same pointing and rejects the high counts that occur in only one of the frames. It was possible to apply this procedure to all the fields, because we had at least two images per filter for each pointing. The Source Extractor code (Bertin & Arnouts 1996) was then used to detect starlike objects exceeding the local background by more than 3.5 σ in the F555W images. Then aperture photometry was performed, using the same positions in all the filters. Slight recentering (less than 2 pixels) from the F555W position was needed to optimize centering of the objects from filter to filter. We performed the photometry with the PHOT task in the DAOPHOT/IRAF package, using the source list

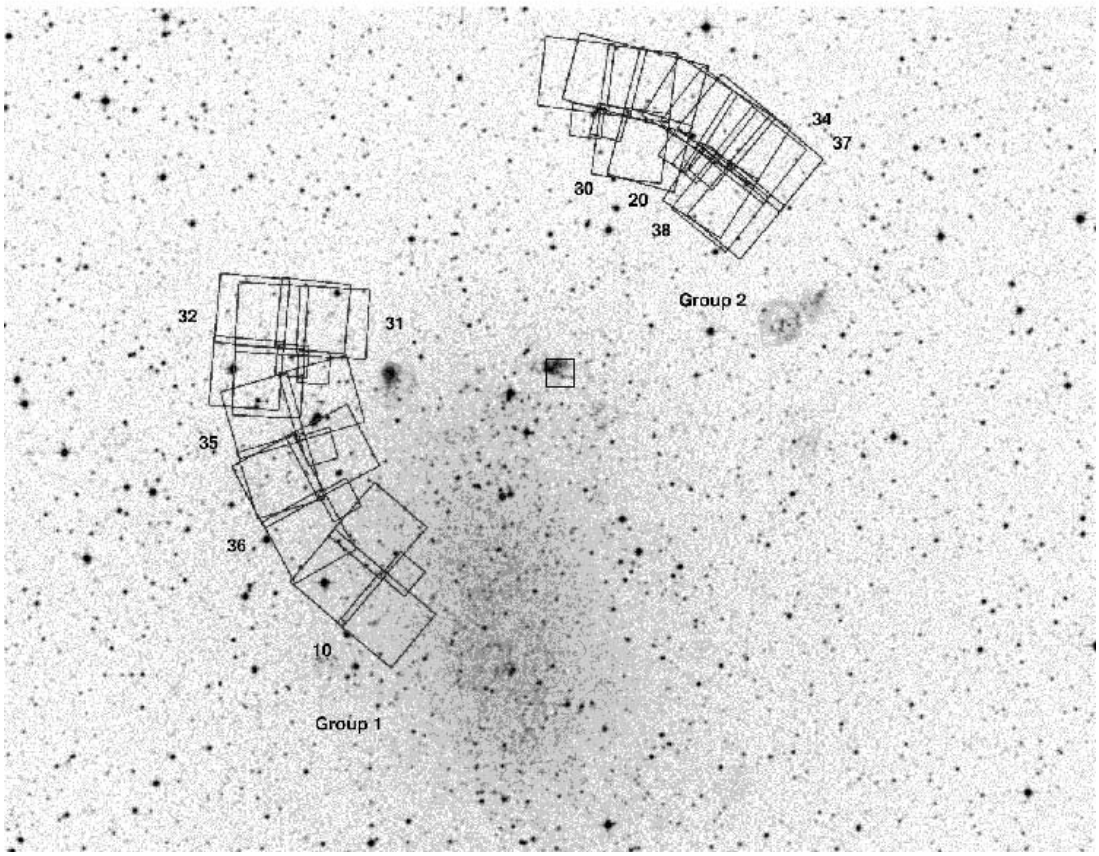

FIG. 1.—Ground-based *V*-band image ($\approx 21' \times 16'$) of NGC 6822 with outlined WFPC2 and STIS fields. North is up, and east is to the left. The small square between the two WFPC2 groups indicates the STIS field.

and positions from Source Extractor. The aperture chosen for both PC and WF chips was 3 pixels, and the sky was measured in an annulus with inner and outer radii of 5 and 8 pixels, respectively. Aperture corrections to a 0.″5 aperture were measured using isolated stars separately for the different chips and filters. Aperture photometry was chosen over point-spread function photometry to ensure a uniform procedure among our fields and to be consistent with previous works. Crowding effects are negligible in our fields. The WFPC2 fields in particular contain fairly sparse populations (the most crowded region is shown in Fig. 5), and the only crowded region, Hubble V, was observed with STIS at UV wavelengths, where crowding is much less than at optical wavelengths. The flux calibration was performed following Holtzman et al. (1995a, 1995b) with the refinements of Dolphin (2000), and included the following steps: (1) *Distortion correction*.—Geometric distortion affects the integration in the photometric aperture. To account for this effect our images were multiplied by the correction image provided by Holtzman et al. (1995b). (2) *Correction for contamination*.—Due to contaminant buildup on the cold CCD plate, the UV throughput decreases. The photometric correction to be applied depends on the time elapsed since the last decontamination procedure. Decontamination correction coefficients were taken from McMaster & Whitmore (2002). (3) *Charge transfer efficiency correction*.—The formula of Dolphin (2000) was applied.

The magnitudes were then transformed into the *HST* VEGAMAG photometric system by applying the zero points as follows: for F336W, F439W, and F555W we used the zero points from Dolphin's Web site,[4] which are relative to a 0.″5 aperture. The zero points for F170W and F255W were taken from the *HST* Data Handbook for WFPC2 with a 0.1 mag correction for the transition from an infinite to a 0.″5 aperture. For our analysis we used the VEGAMAG WFPC2 photometric system, but in Table 3 (the hottest stars) the F336W, F439W, and F555W magnitudes are also transformed to the Johnson *UBV* system to allow comparisons with other works. The error versus magnitude plots of a typical field (field 10) for all the filters used are shown in Figure 2. Such diagrams are used to estimate the magnitude limits of our sample after we impose error cuts for the analysis described in § 3.

The overlapping fields were processed separately, and photometry was performed in each field independently. The measured magnitudes of stars included in several fields are consistent within the errors. The magnitude given in the final catalog is an error-weighted average of all the measurements for the same star. The formula used is

$$\overline{m} = \frac{\sum_{i=1}^{n} m_i/\Delta m_i^2}{\sum_{i=1}^{n} 1/\Delta m_i^2},$$

where n is the number of overlapping fields in which the star is present. The corresponding error is calculated as $\overline{\Delta m} = (\sum_{i=1}^{n} 1/\Delta m_i^2)^{-1/2}$.

The deepest observations are in the F555W band, in which 18,244 stars are detected (above 3.5 σ); 12,423 (70%) of them have photometric accuracy better than 0.2 mag. The number of stars with errors smaller than 0.2 mag in the F439W filter is 1757, and in F336W the number of stars with accuracy better than 0.2 mag is only 535 (2.7% of the stars detected in F555W). Fewer stars are detectable in F170W and F255W with accuracy

[4] See http://purcell.as.arizona.edu/wfpc2_calib.

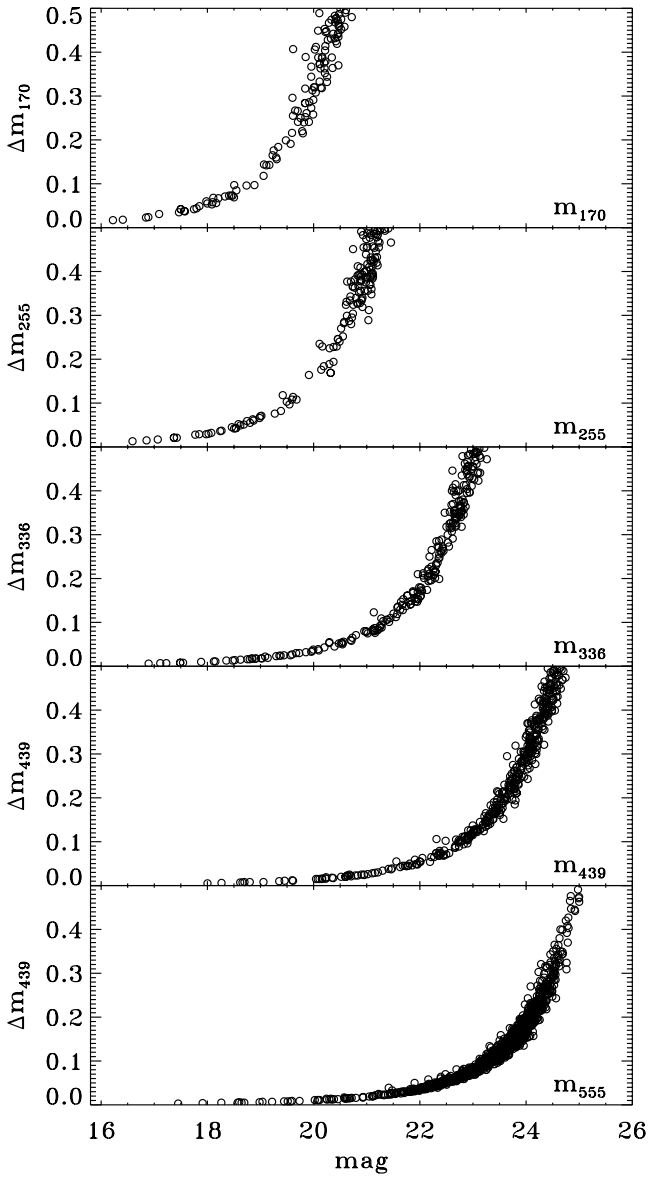

FIG. 2.—Error-magnitude diagrams for the WFPC2 photometry. The data are from a field with long exposures; fields with shorter individual exposures mostly overlap; thus, the combined magnitudes for the objects in these fields have errors comparable to those for objects in a single field with longer exposures.

better than 0.2 mag. See Table 2 for details on errors and magnitude limits in the different filters.

2.2. *STIS Imaging*

Four overlapping STIS images were taken with the 25MAMA aperture using the FUV-MAMA and NUV-MAMA photon-counting detectors. All the images are centered at R.A. $\approx 19^{h}44^{m}52^{s}.2$, decl. $\approx -14^{\circ}43'14''.5$ and cover a $25'' \times 25''$ (60 pc $\times$ 60 pc) field of view. The size of the detectors is 1024×1024 pixels, and the resolution is $0''.024$ pixel^{-1} (0.06 pc), providing the highest resolution view of the compact H II region Hubble V to date. Details about the images are listed in Table 1. The STIS data were downloaded after being calibrated through the Space Telescope Science Institute *calstis* pipeline. Aperture photometry (5 pixels) was performed using the PHOT task in the DAOPHOT/IRAF package. The aperture corrections were measured from 20.8 pixel aperture (corresponding to $0''.5$) photometry of selected stars. The measured magnitudes were converted to the *HST* VEGAMAG system. There are 80 stars detected in both near-UV (NUV) and far-UV (FUV). The magnitude-error diagram is shown in Figure 3, and the magnitude limits are listed in Table 2. Our entire STIS field is included in WFPC2 field 1 of Bianchi et al. (2001b). This previous work provides photometry in four WFPC2 filters, F555W, F439W, F336W, and F255W, which is be combined with the UV STIS photometry in the analysis described in § 3. The STIS images contain the OB 8 association (Hodge 1977) embedded in the H II region Hubble V. The STIS imaging provides a gain of over 2 mag in NUV with respect to the earlier WFPC2 data, and the first observations of this region in the FUV. We have six-band photometry (four bands from Bianchi et al. [2001b] WFPC2 photometry and two from our STIS photometry) for 72 out of the 80 stars detected in our STIS imaging.

3. ANALYSIS: THE STELLAR POPULATIONS

In this section we analyze the multiband photometry of individual stars and derive their physical parameters by comparison with model colors. Two methods are used, and the results are compared. For the stars with good photometric measurements in all the filters, we fit all the observed colors with model colors, to which various reddening amounts are applied, and derive simultaneously stellar $T_{\rm eff}$ and interstellar extinction. For the stars not detected in the UV filters, or with large uncertainties in the UV-band measurements, we use a method similar to the traditional "reddening-free" Q-index.

3.1. *The WFPC2 Photometry: Foreground Contamination*

The observational color-magnitude diagrams in the F336W, F439W, and F555W filters are shown in Figure 4 for all stars in the group 1 fields (*open circles*) and in the group 2 fields (*filled circles*). The dashed lines indicate the magnitude limits of the "restricted sample" analyzed in the following sections.

As described in earlier studies, a "blue plume" is present at $(B - V) \approx 0$ (see, e.g., Bianchi et al. 2001b), indicating H-burning massive stars, especially prominent in the group 1 population. There are a few blue stars in the outer parts of NGC 6822 (group 2 fields). Most of the blue stars in our sample are found in the group 1 fields, which are closer to the main body of the galaxy. The majority of the blue stars are located in the WF3 chip of field 36, shown in Figure 5. This field contains most of the association OB 15 identified by Hodge (1977). There are 47 blue stars with good photometry in all five filters, 46 of them in the group 1 fields and only one in the group 2 fields. Their photometry is given in Table 3.

The majority of red and intermediate-color stars in our sample are expected to be foreground contamination at the latitude of NGC 6822. The model of Ratnatunga & Bahcall (1985) predicts most of the foreground stars in the direction of NGC 6822 with observed magnitudes $17 \leq m_V \leq 22$ to have $0.8 \leq (B - V) \leq 1.3$, which is the area of the H-R diagram where most of the stars from the group 2 fields are found. For the brighter magnitudes there is excellent agreement between the expected number of foreground stars in a given color and visual magnitude range and the number of group 2 stars with the same colors and magnitudes, but at fainter magnitudes the number of stars measured exceeds the number of predicted foreground stars (Fig. 6). The number of foreground stars given in the figure is calculated from the model of Ratnatunga & Bahcall (1985) for an area of 13 arcmin^2 (as covered by our group 2 fields), and the number of stars detected in each bin is also reported. For magnitudes above the limits of our

TABLE 2
MAGNITUDE LIMITS AND NUMBER OF STARS FOR DIFFERENT PHOTOMETRIC ERROR LIMITS

ERROR (mag)	MAGNITUDE LIMIT (NUMBER OF STARS)						
	WFPC2					STIS	
	F170W	F255W	F336W	F439W	F555W	FUV-MAMA	NUV-MAMA
<0.2	19.6 (105)	20.5 (100)	22.3 (536)	23.7 (1757)	24.0 (12423)	22.0 (79)	22.5 (80)
<0.1	18.6 (54)	19.5 (57)	21.4 (269)	22.8 (616)	23.3 (4946)	21.5 (61)	22.5 (80)
<0.05	17.8 (19)	18.5 (23)	20.3 (129)	21.8 (302)	22.3 (1386)	20.5 (45)	21.5 (67)

restricted sample (§ 3.2) there is good agreement, suggesting that most stars in group 2 are foreground; therefore, we can use the group 2 sample to estimate the foreground contamination in the group 1 sample, above $V \approx 22$. At fainter magnitudes we detect significantly more objects than predicted by the Ratnatunga & Bahcall (1985) model. However, these authors warn that for $20 > |b| > 10$ or $V > 22$, their model should be used with caution because these regions are outside the Galactic latitudes or apparent magnitudes tested. We cannot establish with our present sample whether the excess of faint stars [up to 7 times more stars detected than predicted for $(B - V) < 0.8$ and $21 > V > 23$] is due to an old population in the outskirts of NGC 6822, or whether the model of Ratnatunga & Bahcall (1985) needs to be significantly revised in this magnitude range. The question could be clarified by deep imaging with a ground-based telescope.

Using the color-magnitude diagram of the group 2 sample to estimate the foreground contamination of the group 1 sample, we find that the majority (≈70%) of the intermediate-color stars $[0.8 \leq (B - V) \leq 1.3]$ are foreground objects. The fraction drops to ≈30% for stars with bluer color $[0.3 \leq (B - V) \leq 0.8]$ and is negligible at $B - V \approx 0$. We conclude that foreground stars are a significant contamination in the red part of the color-magnitude diagram (both from the Ratnatunga & Bahcall model and by using our group 2 fields as a proxy for the foreground stars estimate), while they do not affect the estimate of the hot massive stars [$(B - V) \approx 0$] content.

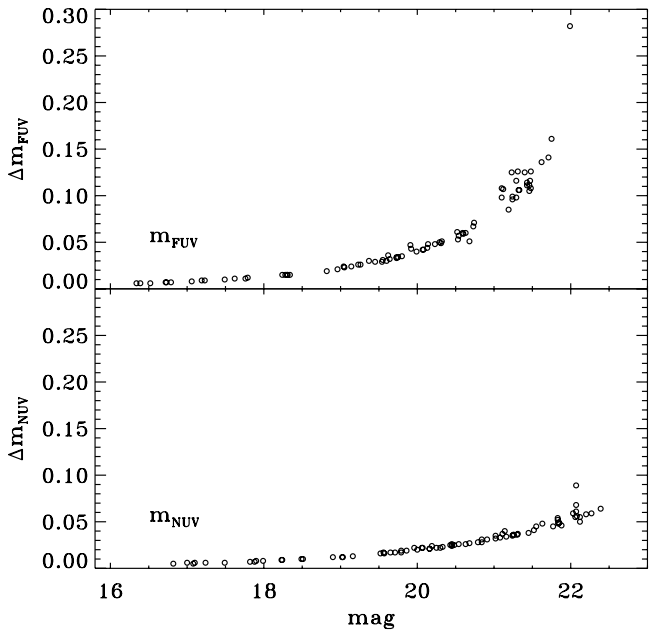

FIG. 3.—Error-magnitude diagrams for the STIS photometry.

3.2. *Derivation of Stellar Parameters*

Here we use the observed photometry to determine the stellar physical parameters. In the first method, known as the "*Q*-method," we construct reddening-free indexes (Q) using different combinations of two colors to determine the amount of reddening and the stellar temperature concurrently. This method is applicable to all stars that have good measurements in at least three photometric bands. In the second method we determine the values of $E(B - V)$ and $T_{\rm eff}$ using all available bands by simultaneous fitting of the observed colors to synthetic colors using χ^2 minimization. For this purpose we use both a modified version of the Bianchi et al. (2001b), Romaniello (1998) code and the CHORIZOS code by Maíz-Apellaniz (2004). Both codes give consistent results. This method is applicable to stars with good photometry in four or more bands.

To describe the analysis with the reddening-free-index method, we first consider photometry in the F336W, F439W, and F555W filters, since our data reach fainter magnitudes in these bands (Fig. 2). We limit the analysis to stars with photometric errors of 0.05, 0.08, and 0.10 mag in F555W, F439W, and F336W, respectively (restricted sample). The error on the reddening-free index, and hence on the derived parameters, is a combination of the errors in the three bands. We applied a progressively less stringent error cut from the *V*-band to the *U*-band measurements in order to approximately match the depth of the sample in these three bands for the blue plume and still have an overall good accuracy of the Q-index. The blue plume has average colors of $(m_{439} - m_{555}) \approx 0.2$ and $(m_{336} - m_{439}) \approx -1.2$; therefore, the same "depth" of the sample is reached for $m_{336} \approx m_{439} - 1.2 \sim m_{555} - 1$. Our chosen error cut of 0.1 mag for the m_{336} magnitudes limits the m_{336} measurements to ∼21.5 mag (Fig. 2). The corresponding error limits in m_{439} and m_{555} are 0.08 and 0.05 mag, respectively, for our restricted sample. These error limits combined translate into a maximum uncertainty for the reddening-free index of $Q_{\rm err} < 0.16$, which propagates into errors on the derived parameters according to the parameters regime, as can be seen in Figure 7. The restricted sample defined above is hence limited to $m_{555} \sim 22.5$ mag, and the number of objects to 230. For red supergiants, having $(m_{439} - m_{555}) \approx 1$ and $(m_{336} - m_{439}) \approx 0-0.5$, the limit of our restricted sample becomes $m_{555} \sim 20.5-21.0$ mag, basically driven by the *U*-band error cut of 0.1 mag. We also consider a less restrictive sample ("wider sample"), with error limits of 0.17, 0.11, and 0.07 mag in m_{336}, m_{439}, and m_{555}, respectively ($Q_{\rm err} < 0.24$), which increases the number of objects by 130 stars and extends the limit to $m_{555} \sim 23$ mag. The total number of objects in the wider sample is therefore 360; values of $T_{\rm eff}$ and $E(B - V)$ from the analysis described below are given in Table 3 (machine-readable version) for 345 stars of this sample; the remaining 15 objects have colors in the range in which the Q-method is not applicable (Q is not reddening free) and are

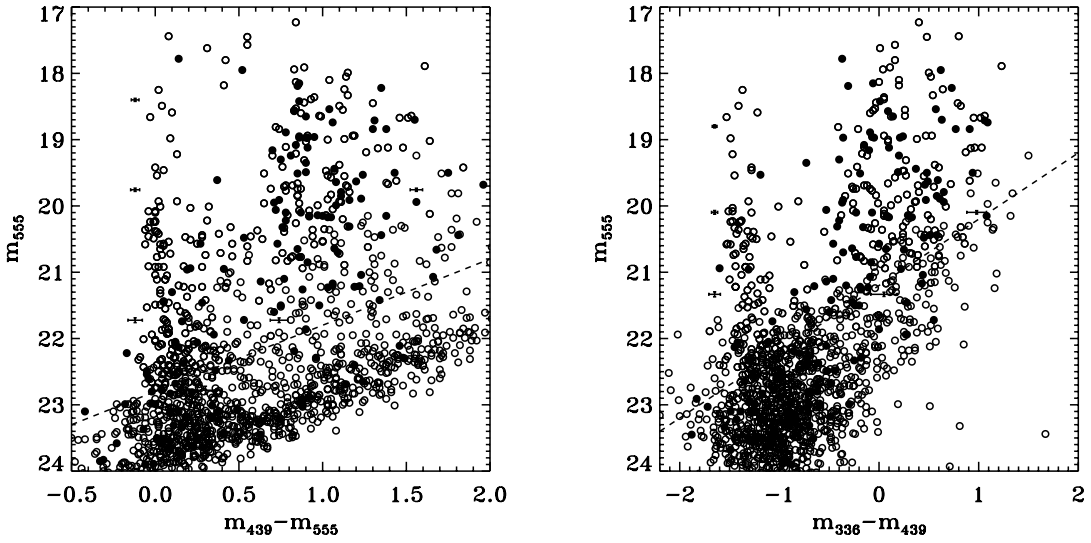

FIG. 4.—Color-magnitude diagrams for stars measured in the WFPC2 fields with the F336W, F439W, and F555W filters. Stars in the group 1 fields are indicated with open circles, and stars in group 2 fields with filled circles. Typical errors for representative values of magnitude and color are shown. The dashed lines indicate the magnitude limits imposed by a photometry error cut of <0.1, <0.08, and <0.05 mag in F336W, F439W, and F555W, respectively, showing the limit of our restricted sample for the analysis described in § 3.

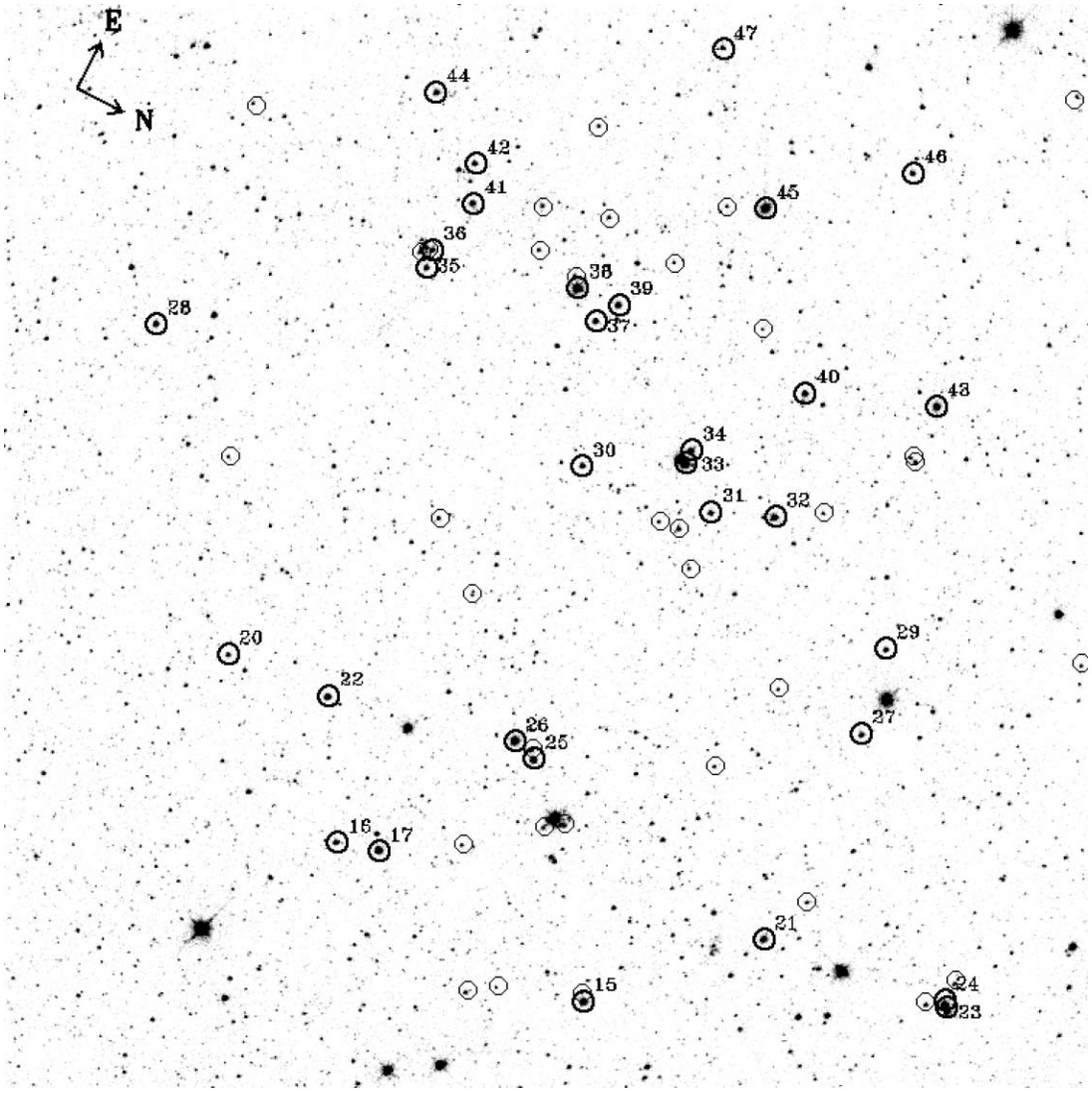

FIG. 5.—WFPC2 image of OB 15 in the F555W band (field 36, WF3 chip, 80″ on a side). The stars detected in all five bands (F170W, F255W, F336W, F439W, and F555W) are indicated with thick circles, and their identification from Table 3 is given. The thin circles indicate hot stars with good photometry in only three filters ($m_{336} - m_{439} < -1$ and $m_{439} - m_{555} < 0$).

TABLE 3

WFPC2 Photometry for the Hottest Stars

Number	R.A. (J2000.0)	Decl. (J2000.0)	m_{555}	m_{439}	m_{336}	m_{255}	m_{170}	V	B	U	$E(B-V)$	$T_{\rm eff}$ (K)
BE_WFPC2_1.....	19 44 37.145	−14 39 49.48	20.94 ± 0.03	21.15 ± 0.04	19.55 ± 0.04	19.00 ± 0.11	19.09 ± 0.20	20.93	21.15	20.22	0.32 ± 0.03	42700^{+7500}_{-4900}
BE_WFPC2_2.....	19 45 03.565	−14 46 14.96	21.11 ± 0.03	21.12 ± 0.03	19.98 ± 0.04	19.93 ± 0.09	19.75 ± 0.12	21.11	21.12	20.48	0.27 ± 0.05	22600^{+3000}_{-1900}
BE_WFPC2_3.....	19 45 06.802	−14 47 04.43	20.39 ± 0.03	20.40 ± 0.03	19.14 ± 0.03	18.93 ± 0.05	18.70 ± 0.05	20.39	20.40	19.69	0.27 ± 0.04	26200^{+3000}_{-1900}
BE_WFPC2_4.....	19 45 06.989	−14 47 01.86	21.32 ± 0.03	21.35 ± 0.04	20.13 ± 0.04	19.99 ± 0.10	19.81 ± 0.14	21.32	21.35	20.66	0.30 ± 0.06	26800^{+4000}_{-2900}
BE_WFPC2_5.....	19 45 08.502	−14 47 09.98	20.42 ± 0.03	20.44 ± 0.03	19.01 ± 0.03	18.70 ± 0.05	18.25 ± 0.05	20.42	20.44	19.62	0.29 ± 0.04	41200^{+5000}_{-7400}
BE_WFPC2_6.....	19 45 08.604	−14 46 26.46	21.05 ± 0.03	21.12 ± 0.03	20.02 ± 0.04	20.13 ± 0.12	19.80 ± 0.13	21.05	21.12	20.50	0.31 ± 0.06	22700^{+3000}_{-1900}
BE_WFPC2_7.....	19 45 09.247	−14 45 51.89	20.24 ± 0.03	20.21 ± 0.03	18.72 ± 0.03	18.39 ± 0.05	18.03 ± 0.06	20.24	20.21	19.35	0.25 ± 0.03	36900^{+7500}_{-2900}
BE_WFPC2_8.....	19 45 09.408	−14 47 10.14	21.49 ± 0.03	21.52 ± 0.04	20.27 ± 0.05	20.15 ± 0.12	19.69 ± 0.11	21.49	21.52	20.81	0.28 ± 0.07	29700^{+10500}_{-3900}
BE_WFPC2_9.....	19 45 10.140	−14 44 12.39	21.71 ± 0.04	21.76 ± 0.05	20.49 ± 0.06	20.24 ± 0.20	19.55 ± 0.19	21.71	21.76	21.04	0.27 ± 0.08	33400^{+14000}_{-6900}
BE_WFPC2_10.....	19 45 11.411	−14 44 24.89	20.92 ± 0.03	20.92 ± 0.03	19.63 ± 0.04	19.07 ± 0.08	18.82 ± 0.10	20.92	20.92	20.19	0.16 ± 0.05	24900^{+4000}_{-1900}
BE_WFPC2_11.....	19 45 11.836	−14 44 22.31	20.46 ± 0.03	20.42 ± 0.03	19.13 ± 0.03	18.78 ± 0.06	18.42 ± 0.07	20.46	20.42	19.69	0.18 ± 0.05	24900^{+2000}_{-2900}
BE_WFPC2_12.....	19 45 12.206	−14 46 59.01	20.72 ± 0.03	20.81 ± 0.03	19.37 ± 0.03	19.32 ± 0.09	18.90 ± 0.10	20.71	20.81	19.98	0.37 ± 0.03	42400^{+5000}_{-7400}
BE_WFPC2_13.....	19 45 12.229	−14 46 58.89	20.77 ± 0.03	20.78 ± 0.03	19.48 ± 0.03	19.51 ± 0.07	19.16 ± 0.10	20.77	20.78	20.04	0.36 ± 0.05	34300^{+9500}_{-5900}
BE_WFPC2_14.....	19 45 12.250	−14 44 47.56	19.93 ± 0.02	19.95 ± 0.03	18.64 ± 0.03	18.55 ± 0.05	18.10 ± 0.06	19.93	19.95	19.20	0.36 ± 0.05	39400^{+7500}_{-9900}
BE_WFPC2_15.....	19 45 12.657	−14 45 0028	19.42 ± 0.02	19.42 ± 0.03	18.14 ± 0.03	18.02 ± 0.04	17.80 ± 0.05	19.42	19.42	18.69	0.32 ± 0.04	28900^{+4000}_{-2900}
BE_WFPC2_16.....	19 45 12.768	−14 45 20.39	20.92 ± 0.03	20.97 ± 0.03	19.63 ± 0.03	19.39 ± 0.09	19.06 ± 0.12	20.92	20.97	20.21	0.31 ± 0.05	35000^{+12000}_{-4900}
BE_WFPC2_17.....	19 45 12.827	−14 45 17.53	19.46 ± 0.02	19.51 ± 0.03	18.23 ± 0.03	17.98 ± 0.04	18.08 ± 0.06	19.46	19.51	18.78	0.32 ± 0.04	27100^{+4000}_{-900}
BE_WFPC2_18.....	19 45 12.972	−14 43 0083	20.36 ± 0.03	20.30 ± 0.03	18.89 ± 0.03	18.61 ± 0.06	17.90 ± 0.05	20.36	20.30	19.49	0.27 ± 0.04	45100^{+2500}_{-7400}
BE_WFPC2_19.....	19 45 13.001	−14 43 0080	20.24 ± 0.03	20.24 ± 0.03	18.84 ± 0.03	18.66 ± 0.05	18.19 ± 0.06	20.24	20.24	19.44	0.32 ± 0.04	41000^{+5000}_{-8400}
BE_WFPC2_20.....	19 45 13.310	−14 45 32.98	21.49 ± 0.03	21.49 ± 0.04	20.12 ± 0.04	19.68 ± 0.11	19.57 ± 0.19	21.49	21.49	20.71	0.24 ± 0.06	32200^{+10000}_{-3900}
BE_WFPC2_21.....	19 45 13.319	−14 44 51.42	20.08 ± 0.03	20.08 ± 0.03	18.61 ± 0.03	18.27 ± 0.04	17.85 ± 0.05	20.08	20.08	19.23	0.27 ± 0.03	39200^{+5000}_{-6900}
BE_WFPC2_22.....	19 45 13.356	−14 45 25.61	20.08 ± 0.03	20.04 ± 0.03	18.53 ± 0.03	18.24 ± 0.04	17.75 ± 0.05	20.08	20.04	19.17	0.27 ± 0.03	41500^{+5000}_{-7400}
BE_WFPC2_23.....	19 45 13.435	−14 44 38.02	20.24 ± 0.03	20.23 ± 0.03	18.84 ± 0.03	18.69 ± 0.06	18.11 ± 0.07	20.24	20.23	19.43	0.33 ± 0.04	43000^{+5000}_{-7400}
BE_WFPC2_24.....	19 45 13.459	−14 44 38.39	19.22 ± 0.02	19.35 ± 0.02	17.88 ± 0.02	17.77 ± 0.04	17.47 ± 0.04	19.21	19.35	18.50	0.39 ± 0.03	42000^{+5000}_{-4900}
BE_WFPC2_25.....	19 45 13.551	−14 45 11.10	20.03 ± 0.03	20.24 ± 0.03	18.77 ± 0.03	18.62 ± 0.05	18.48 ± 0.08	20.02	20.24	19.39	0.41 ± 0.03	41600^{+5000}_{-7400}
BE_WFPC2_26.....	19 45 13.590	−14 45 12.82	18.98 ± 0.02	19.07 ± 0.02	17.58 ± 0.02	17.42 ± 0.03	16.84 ± 0.03	18.97	19.07	18.21	0.35 ± 0.01	48300^{+0}_{-4900}
BE_WFPC2_27.....	19 45 14.388	−14 44 52.07	20.92 ± 0.03	20.94 ± 0.03	19.60 ± 0.04	19.27 ± 0.08	18.89 ± 0.10	20.92	20.94	20.18	0.26 ± 0.06	32300^{+10000}_{-3900}
BE_WFPC2_28.....	19 45 14.529	−14 45 47.99	20.38 ± 0.03	20.38 ± 0.03	19.06 ± 0.03	18.80 ± 0.06	18.45 ± 0.08	20.38	20.38	19.63	0.26 ± 0.05	29500^{+6000}_{-2900}
BE_WFPC2_29.....	19 45 14.797	−14 44 53.35	21.04 ± 0.03	21.04 ± 0.03	19.66 ± 0.04	19.49 ± 0.10	19.17 ± 0.14	21.04	21.04	20.25	0.30 ± 0.05	35800^{+10000}_{-5900}
BE_WFPC2_30.....	19 45 14.889	−14 45 17.63	20.65 ± 0.03	20.68 ± 0.03	19.32 ± 0.03	18.85 ± 0.07	18.55 ± 0.09	20.65	20.68	19.90	0.22 ± 0.05	29900^{+6000}_{-2900}
BE_WFPC2_31.....	19 45 14.978	−14 45 08.35	21.11 ± 0.03	21.17 ± 0.04	19.98 ± 0.04	19.59 ± 0.11	19.33 ± 0.19	21.11	21.17	20.50	0.24 ± 0.06	24200^{+3000}_{-2900}
BE_WFPC2_32.....	19 45 15.103	−14 45 04.31	20.10 ± 0.03	20.10 ± 0.03	18.82 ± 0.03	18.50 ± 0.05	18.33 ± 0.07	20.10	20.10	19.37	0.24 ± 0.04	25700^{+3000}_{-1900}
BE_WFPC2_33.....	19 45 15.125	−14 45 11.46	18.59 ± 0.02	18.69 ± 0.02	17.47 ± 0.02	17.37 ± 0.03	17.50 ± 0.05	18.58	18.69	18.00	0.39 ± 0.04	26900^{+3000}_{-900}
BE_WFPC2_34.....	19 45 15.193	−14 45 11.53	20.57 ± 0.03	20.62 ± 0.03	19.10 ± 0.03	18.87 ± 0.06	18.21 ± 0.07	20.57	20.62	19.74	0.30 ± 0.02	45800^{+2500}_{-4900}
BE_WFPC2_35.....	19 45 15.367	−14 45 33.47	21.11 ± 0.03	21.17 ± 0.04	19.67 ± 0.04	19.55 ± 0.10	19.23 ± 0.17	21.11	21.17	20.30	0.33 ± 0.03	41600^{+5000}_{-7400}
BE_WFPC2_36.....	19 45 15.454	−14 45 33.65	21.22 ± 0.03	21.39 ± 0.04	19.95 ± 0.04	19.61 ± 0.12	19.25 ± 0.18	21.21	21.39	20.56	0.36 ± 0.04	41700^{+5000}_{-7400}
BE_WFPC2_37.....	19 45 15.521	−14 45 21.51	20.58 ± 0.03	20.52 ± 0.03	19.03 ± 0.03	18.75 ± 0.06	18.17 ± 0.06	20.58	20.52	19.66	0.25 ± 0.04	41900^{+5000}_{-7400}
BE_WFPC2_38.....	19 45 15.618	−14 45 23.69	18.66 ± 0.02	18.63 ± 0.02	17.10 ± 0.02	16.85 ± 0.03	16.41 ± 0.03	18.66	18.63	17.75	0.28 ± 0.03	40000^{+5000}_{-4900}
BE_WFPC2_39.....	19 45 15.638	−14 45 20.66	20.23 ± 0.03	20.23 ± 0.03	18.76 ± 0.03	18.46 ± 0.05	18.10 ± 0.06	20.23	20.23	19.38	0.28 ± 0.03	38000^{+7500}_{-4400}
BE_WFPC2_40.....	19 45 15.685	−14 45 06.49	20.33 ± 0.03	20.29 ± 0.03	18.84 ± 0.03	18.54 ± 0.05	18.00 ± 0.06	20.33	20.29	19.46	0.27 ± 0.04	41800^{+5000}_{-7400}
BE_WFPC2_41.....	19 45 15.737	−14 45 32.75	20.60 ± 0.03	20.65 ± 0.03	19.29 ± 0.03	19.02 ± 0.07	18.41 ± 0.08	20.60	20.65	19.87	0.31 ± 0.05	42300^{+5000}_{-11900}
BE_WFPC2_42.....	19 45 15.908	−14 45 33.89	20.91 ± 0.03	20.87 ± 0.03	19.43 ± 0.03	19.00 ± 0.07	18.74 ± 0.10	20.91	20.87	20.04	0.22 ± 0.05	33400^{+8000}_{-3900}
BE_WFPC2_43.....	19 45 15.922	−14 44 58.13	19.54 ± 0.02	19.55 ± 0.03	18.10 ± 0.03	17.85 ± 0.04	17.56 ± 0.04	19.54	19.55	18.72	0.30 ± 0.02	35200^{+3500}_{-1900}
BE_WFPC2_44.....	19 45 16.115	−14 45 38.47	20.58 ± 0.03	20.61 ± 0.03	19.08 ± 0.03	18.59 ± 0.06	17.98 ± 0.06	20.58	20.61	19.73	0.23 ± 0.03	44800^{+5000}_{-4900}
BE_WFPC2_45.....	19 45 16.366	−14 45 14.88	18.49 ± 0.02	18.53 ± 0.02	17.12 ± 0.02	17.07 ± 0.03	16.89 ± 0.03	18.49	18.53	17.72	0.38 ± 0.01	34300^{+1000}_{-900}
BE_WFPC2_46.....	19 45 16.832	−14 45 07.13	20.74 ± 0.03	20.78 ± 0.03	19.32 ± 0.03	18.98 ± 0.07	18.50 ± 0.10	20.74	20.78	19.94	0.29 ± 0.04	41500^{+5000}_{-7400}
BE_WFPC2_47.....	19 45 16.941	−14 45 22.50	21.27 ± 0.03	21.30 ± 0.04	19.98 ± 0.04	19.42 ± 0.12	19.11 ± 0.14	21.27	21.30	20.55	0.21 ± 0.06	29400^{+10500}_{-2900}

Notes.—Units of right ascension are hours, minutes, and seconds, and units of declination are degrees, arcminutes, and arcseconds. The stars with measurements in all five WFPC2 bands are given here. The photometry for the entire sample is available in the electronic edition of the *Astronomical Journal*. The first star is in the "group 2" fields, and all the others are in the "group 1" fields. Magnitudes are in the VEGAMAG system.

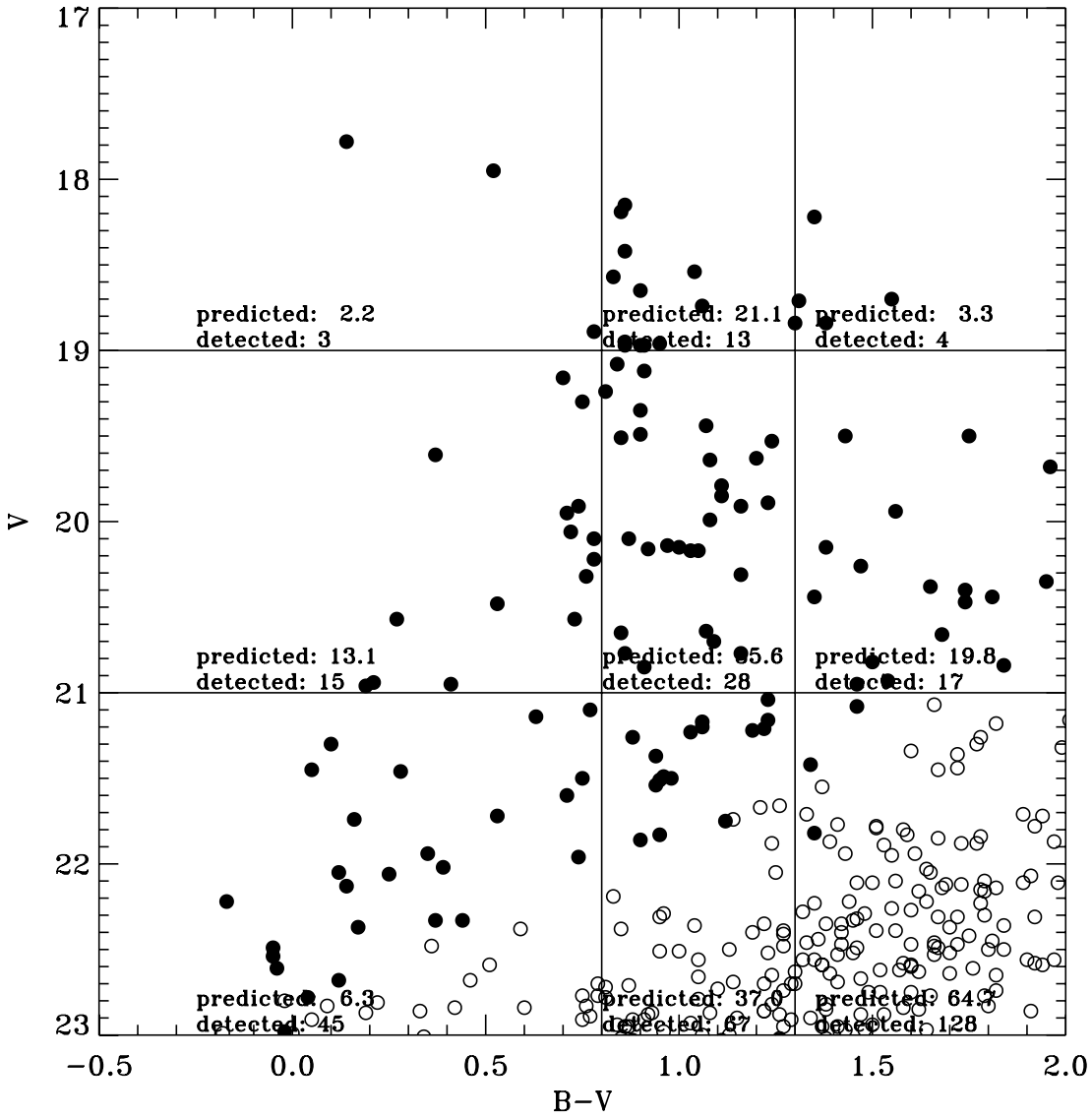

FIG. 6.—Color-magnitude diagram of stars detected in the group 2 fields with the number of foreground stars per color-magnitude bin predicted by the Ratnatunga & Bahcall (1985) model in a 13 arcmin^2 area. There is agreement between the number of stars in group 2 and the expected amount of foreground stars, except for the fainter magnitude bins, indicating that at the galactocentric distance of these fields the stellar objects detected (brighter than the magnitude limits of our restricted sample) are essentially foreground MW stars. The excess of detected objects in the fainter magnitude bins may be due to the uncertainty of the Ratnatunga & Bahcall (1985) models for magnitudes fainter than $V \sim 22$. Filled circles are the wider sample analyzed in § 3.2.

probably foreground cool stars. Table 2 gives the number of objects in each filter within given error limits.

The reddening-free Q-index is a combination of two different colors (usually from three bands) with the ratio of the two color excesses, so that its value does not depend on the reddening. The classical Q-index is constructed with magnitudes in U, B, and V (e.g., Massey 1998a),

$$\begin{aligned} Q_{UBV} &= (U-B) - \frac{E(U-B)}{E(B-V)}(B-V) \\ &= (U-B)_0 + E(U-B) \\ &\quad - \frac{E(U-B)}{E(B-V)}[(B-V)_0 + E(B-V)] \\ &= (U-B)_0 - \frac{E(U-B)}{E(B-V)}(B-V)_0 = Q_{UBV0}, \end{aligned}$$

where the subscript $_0$ indicates intrinsic colors. A similar index can be constructed for any combination of at least three filters. The observed value of Q is equal to the intrinsic one; hence, it provides a reddening-independent direct measurement of $T_{\rm eff}$, to the extent that the ratio $C = E(U-B)/E(B-V)$ is actually constant. This is a good approximation for low values of $E(B-V)$. If we were using monochromatic fluxes, C would be constant for any amount of reddening and would only depend on the type of extinction, i.e., on the extinction curve adopted. In practice, when we use broadband filters, because both $T_{\rm eff}$ and reddening variations change the slope of the spectrum within the band, C is constant only within limited ranges of $E(B-V)$ and $T_{\rm eff}$ (see L. Bianchi & A. Tolea 2006, in preparation, for further discussion).

We constructed Q-indexes (as a function of stellar parameters) in the *HST* filter system using a grid of synthetic colors obtained by applying the transmission curves of the WFPC2 filters to Kurucz (1993) synthetic stellar spectra models calculated by

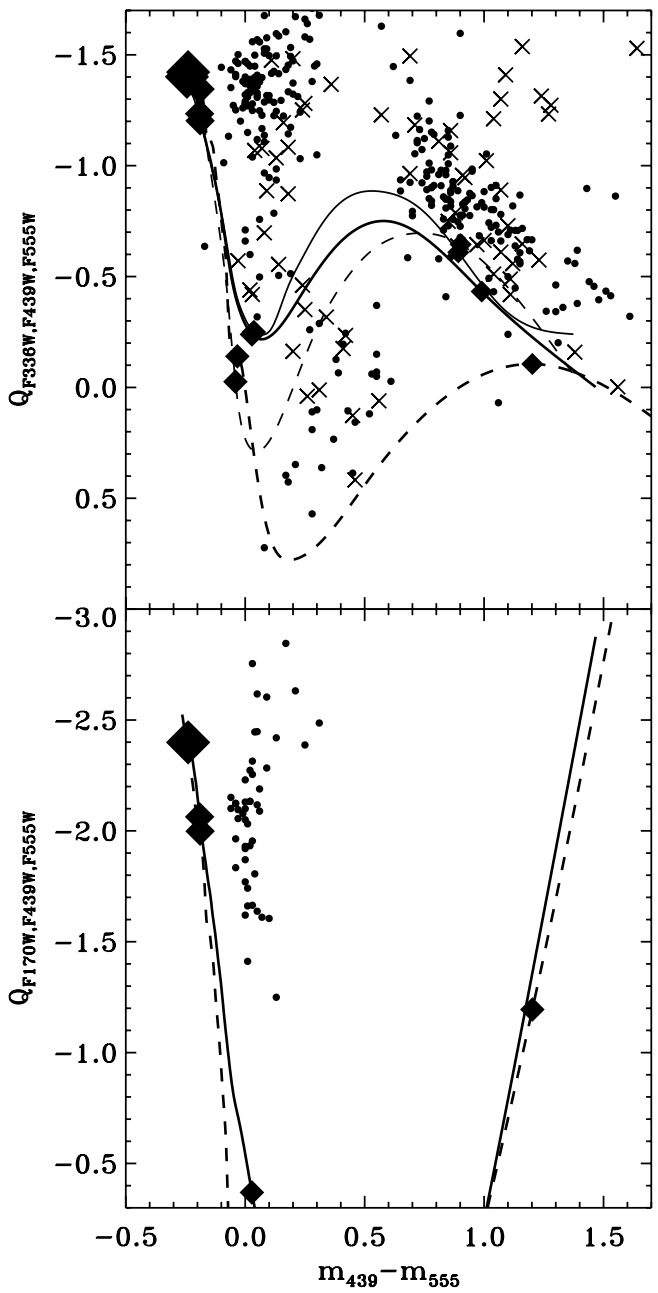

FIG. 7.—*Top*: Reddening-free index $Q_{F336W,F439W,F555W}$ vs. $(m_{439} - m_{555})$. The circles represent our restricted sample, and the crosses show the wider sample. The lines are constructed from model colors for main-sequence stars (*solid lines*) and supergiants (*dashed lines*); thick lines are for solar metallicity, and thin lines for models with $Z = 0.002$. *Bottom*: $Q_{F170W,F439W,F555W}$ vs. $(m_{439} - m_{555})$. The circles represent the stars from our restricted sample that are detected also in the F170W band. The model $Q_{F170W,F439W,F555W}$ values (solar metallicity) for main-sequence and supergiant stars are overplotted as above. Filled diamonds of decreasing size mark models of $T_{\rm eff} = 35{,}000$, 25,000, 10,000, and 5000 K.

Lejeune et al. (1997) and by L. Bianchi et al. (2006, in preparation). Our model colors cover a large range in stellar parameters $T_{\rm eff}$ and $\log g$ for different metallicities. The effects of differing amounts and types of extinction are applied to the model spectra, and synthetic colors are computed applying the filter curves to the reddened models. Therefore, our grids of model colors allow us to also derive the value of C for various types of reddening, and to verify within what limits it actually remains constant. We initially adopt Milky Way (MW)–type extinction ($R_V = 3.1$) assuming that in our sample most of the extinction is due to Milky Way foreground dust, which is confirmed by our results. The MW reddening law ($R_V = 3.1$) was also found appropriate for NGC 6822 by Massey et al. (1995). From our model colors we found $C_{F336W,F439W,F555W}$ to be constant in the temperature range $T_{\rm eff} \in [8000,\ 50{,}000]$ and with $E(B - V) < 0.7$, with a value of $C_{F336W,F439W,F555W} = 0.96$. We use the $Q_{F336W,F439W,F555W}$ index to derive the extinction and the stellar temperatures in these intervals. We can also use $Q_{F336W,F439W,F555W}$ for the stars in the range $T_{\rm eff} \in [5000,\ 8000]$ and $E(B - V) < 0.7$, with $C_{F336W,F439W,F555W} = 0.90$.

Because a higher reddening applied to a hot star spectrum can mimic a less reddened cooler spectrum, in certain parameter ranges the solution $[T_{\rm eff}, E(B - V)]$ is not unique, as can be seen from Figure 7. Since the Q-index is reddening-independent (within the applicable range), on the color-Q diagram the reddening only displaces the points in color (along the x-axis in Fig. 7). The difference in color between the observed points and the model colors (corresponding to the intrinsic colors) provides an estimate of the extinction, while the value of Q provides $T_{\rm eff}$. In the ranges in which, for a given observed color and Q, the intrinsic color has more than one possible value ($Q_{F336W,F439W,F555W} \in [-0.7, -0.2]$, $[m_{439} - m_{555}] > 0.2$ for solar metallicity; see Fig. 7), different solutions for $[T_{\rm eff}, E(B - V)]$ exist.

In Figure 7 (*top*) we plot the synthetic $Q_{F336W,F439W,F555W}$ index versus the color $m_{439} - m_{555}$. The observed values are shown as circles for our restricted sample (stars with error in Q better than 0.16), and as crosses for the wider sample ($0.24 > Q_{\rm err} > 0.16$). The solid lines represent model colors for main-sequence stars (solar metallicity: *thick lines*; $Z = 0.002$: *thin lines*). The model curves show that for $Q_{F336W,\,F439W,\,F555W} \lesssim -0.7$ (the exact value slightly depending on metallicity) there is only one solution; for more positive values of $Q_{F336W,F439W,F555W}$ there are the following possibilities: when $(m_{439} - m_{555}) \leq 0.1$ there is a unique solution for $[E(B - V),\ T_{\rm eff}]$; for stars with $0.1 < (m_{439} - m_{555}) < 0.6$ there are two possible solutions; and for $(m_{439} - m_{555}) > 0.6$ there are three possible solutions. In the case of this study, however, we note that when there is more than one possible solution, the lowest value of $E(B - V)$ is similar to the average $E(B - V)$ in the field. The values of $E(B - V)$ from the other possible solutions significantly exceed any value of $E(B - V)$ determined in these fields for the stars with a unique solution, and exceed by $\sim$0.8 mag the average $E(B - V)$ determined in the galaxy by this and previous works. This difference can be appreciated at a glance from Figure 7. Therefore, we choose the solution $[E(B - V),\ T_{\rm eff}]$ with the lowest extinction value, assuming that there is no reason for the extinction to vary extremely in such sparse fields. For the same reason, for those stars that have $(m_{439} - m_{555}) > 0.5$ and formally a unique solution from the Q-diagram implying $E(B - V) > 0.5$, we adopt instead the average value of $E(B - V) = 0.27$ (as determined from the restricted sample in the field population outside of OB 15) for those stars in the group 1 fields, and $E(B - V) = 0.2$ for those located in the group 2 fields. These objects are seen as a small "plume" above the model Q-curves for red stars in Figure 7 and are identified with flags "c" and "d," respectively, in the machine-readable version of Table 3. Theoretically, they could be hot stars with very high extinction, but the majority are likely foreground stars.

An interesting feature of the color-Q diagram is the separation of the model color curves for different gravities. Main-sequence stars (*solid lines*) and supergiants (*dashed lines*) are plotted in the $T_{\rm eff}$ range of [50,000, 4000] in Figure 7. The curves separate for $T_{\rm eff} \lesssim 10{,}000$ K ($Q > -0.2$). A group of $\approx$25 stars with high

values of Q can be classified as supergiants based on their photometry, indicating that these cooler objects belong to NGC 6822 and are not foreground stars. They are found in the group 1 fields (four in the area of OB 15), and only one or two are found in the group 2 fields.

We have also calculated $Q_{\rm F336W,F439W,F555W}$ using low-metallicity models ($Z = 0.002$; thin lines in Fig. 7 [*top*]) in order to check how metallicity affects the color-Q diagram. The solutions for hot stars (down to 10,000 K) do not differ significantly with metallicity, but for low-temperature stars the results for $E(B-V)$ and $T_{\rm eff}$ depend on metallicity. This paper is focused on the hot massive stellar population of NGC 6822, so the choice of metallicity does not affect our results.

For stars detected also in the UV, we constructed additional Q-indexes including the F170W magnitude, which provides a more sensitive measurement of the high temperatures and especially of the extinction. As shown in Figure 7 (*bottom*), $Q_{\rm F170W,F439W,F555W}$ spans over 2 mag in the $T_{\rm eff}$ range 10,000–35,000 K, compared to the $\sim$1 mag variation of $Q_{\rm F336W,F439W,F555W}$. However, the larger uncertainties in the UV photometry, due to the lower sensitivity of the CCD at UV wavelengths, limit the advantage of this broader wavelength coverage to the hottest objects. We found, from our model colors, $C_{\rm F170W,F439W,F555W} = 4.15$, approximately constant for $T_{\rm eff} \in [11{,}000,\ 50{,}000]$ and $E(B-V) < 0.7$. The model values of $Q_{\rm F170W,F439W,F555W}$ for low-gravity stars are again separate from the dwarfs for temperatures between 10,000 and 8000 K. This part of the diagram is not shown, since only the hottest stars in our sample are detected in F170W. The analysis using five-band photometry is restricted to objects with photometric accuracy in F170W and F255W better than 0.2 mag. There are 47 such stars in the WFPC2 sample. All of the stars with good photometry in five bands lie in the unique-solution part of the color-Q diagrams, and the values of $E(B-V)$ and $T_{\rm eff}$ obtained from different Q-indexes are consistent within the errors.

For our restricted sample, $E(B-V)$ varies between 0.17 and 0.37, with a mean value of 0.27, which is in agreement with the estimate of Massey et al. (1995) for the outer parts of NGC 6822.

In the second method we derive the values of extinction and stellar temperature by simultaneous χ^2 minimization fitting of all the observed colors with the same library of model colors. The advantage of this method is the use of all the available photometric information simultaneously, each magnitude being weighted according to its uncertainty. We used the CHORIZOS code by Maíz-Apellaniz (2004), as well as a code developed by us (based on the method by Romaniello 1998), and found consistent results. We obtain a good fit with $\chi^2 \in [0.6,\ 5.5]$ for approximately 60% of the stars with five-band photometry. Two examples of good fits are shown in Figure 8. The model spectrum that best fits the observed colors is shown along with the model magnitudes and the observed magnitudes with their errors. The derived $T_{\rm eff}$ and $E(B-V)$ correlate well with the values obtained from the Q-method within the errors, although there is a slight trend of higher extinction values, and consequently $T_{\rm eff}$, from the χ^2 fit.

In both the reddening-free and the χ^2 fitting method we used MW-type extinction with $R_V = 3.1$ and also tried UV-steeper extinction laws, such as LMC-type extinction. We found the MW-type extinction to provide a better match to the observed photometry, consistent with the result that most of the extinction is due to foreground MW dust. In order to construct physical H-R diagrams (§ 4), for the stars with five-band photometry we adopt the values of $T_{\rm eff}$ and reddening from the χ^2 fit (Table 3), and for the stars with three good measurements the values from the Q-method. Stars with B and V measurements having errors

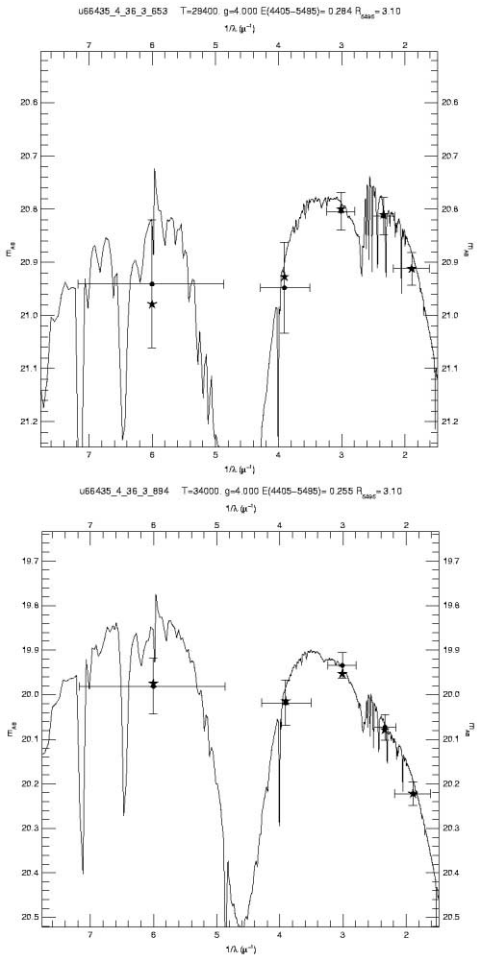

FIG. 8.—Two examples of χ^2 fits obtained with the CHORIZOS code. The crosses show the observed magnitudes with their errors, and the stars show the synthetic magnitudes with the width of the filters. The model spectrum from which the synthetic magnitudes are generated is also shown. The lines appear very strong in the spectrum because of the flux scale in magnitudes.

better than 0.2 mag, but with errors larger than our wider sample limits in other bands, are also included in Table 3 (machine-readable version).

3.3. *STIS Photometry*

Most of the UV sources (72 out of 80) in the STIS imaging of OB 8 have measured counterparts in the WFPC2 photometry of Bianchi et al. (2001b) that provide additional measurements in four bands: F255W, F336W, F439W, and F555W. We derived temperatures and $E(B-V)$ by comparing the photometry to the model colors as described in § 3.2, using χ^2 fitting.

The additional STIS FUV band gives us the opportunity to refine the determination of extinction and temperature with respect to our previous work. The errors in the WFPC2 imaging of Bianchi et al. (2001b) in the F255W and F336W filters are larger than 0.2 mag for more than one-third of the sample, and our new STIS UV photometry with relatively small errors significantly improves the determination of the stellar parameters. The stellar temperatures determined from the χ^2 fit including UV bands tend to be higher than the previous results. The H-R diagram of the Hubble V region is shown in Figure 11 with filled circles. The results from the photometry of Bianchi et al. (2001b) are shown with crosses for comparison. The photometric measurements and derived stellar parameters, as well as the identification with the

TABLE 4

STIS PHOTOMETRY

Name	R.A. (J2000.0)	Decl. (J2000.0)	NUV	FUV	$E(B-V)$	$T_{\rm eff}$ (K)	ID[a]
BE_STIS_1	19 44 51.197	−14 43 08.67	22.03 ± 0.06	21.29 ± 0.12	...	...	...
BE_STIS_2	19 44 51.234	−14 43 09.26	19.96 ± 0.02	19.14 ± 0.02	0.35 ± 0.05	26200^{+2800}_{-2200}	LB-f1-540
BE_STIS_3	19 44 51.308	−14 43 12.65	18.49 ± 0.01	17.79 ± 0.01	0.41 ± 0.01	38500 ± 1000	LB-f1-536
BE_STIS_4	19 44 51.343	−14 43 19.69	17.90 ± 0.01	17.19 ± 0.01	0.40 ± 0.01	37300^{+2700}_{-200}	LB-f1-525
BE_STIS_5	19 44 51.351	−14 43 06.87	22.07 ± 0.06	21.48 ± 0.13	0.43 ± 0.22	23900^{+11100}_{-8900}	LB-f1-555
BE_STIS_6	19 44 51.380	−14 43 08.42	21.63 ± 0.05	21.10 ± 0.10	0.34 ± 0.13	18900^{+5100}_{-2900}	LB-f1-549
BE_STIS_7	19 44 51.387	−14 43 07.07	21.83 ± 0.05	21.40 ± 0.12	0.20 ± 0.15	15000^{+3000}_{-2000}	LB-f1-558
BE_STIS_8	19 44 51.388	−14 43 18.82	21.84 ± 0.05	21.19 ± 0.09	0.11 ± 0.17	14000^{+5000}_{-2000}	LB-f1-527
BE_STIS_9	19 44 51.550	−14 43 19.79	19.16 ± 0.01	18.31 ± 0.01	0.37 ± 0.01	35100^{+4900}_{-1100}	LB-f1-531
BE_STIS_10	19 44 51.630	−14 43 06.44	22.08 ± 0.06	21.43 ± 0.11	0.32 ± 0.21	19100^{+5900}_{-5100}	LB-f1-578
BE_STIS_11	19 44 51.667	−14 43 19.51	19.02 ± 0.01	18.24 ± 0.01	0.40 ± 0.01	36600^{+3400}_{-2600}	LB-f1-535
BE_STIS_12	19 44 51.667	−14 43 13.09	19.71 ± 0.02	18.96 ± 0.02	0.41 ± 0.04	27200^{+2800}_{-3200}	LB-f1-552
BE_STIS_13	19 44 51.681	−14 43 13.61	20.54 ± 0.03	19.73 ± 0.03	0.37 ± 0.08	28900^{+8600}_{-5900}	LB-f1-550
BE_STIS_14	19 44 51.696	−14 43 10.88	20.63 ± 0.03	19.99 ± 0.04	0.31 ± 0.09	21900^{+4100}_{-2900}	LB-f1-566
BE_STIS_15	19 44 51.725	−14 43 18.91	17.10 ± 0.01	16.39 ± 0.01	0.41 ± 0.01	37200^{+2800}_{-300}	LB-f1-539
BE_STIS_16	19 44 51.740	−14 43 16.22	18.90 ± 0.01	18.30 ± 0.01	0.52 ± 0.01	39500^{+3000}_{-2000}	LB-f1-546
BE_STIS_17	19 44 51.747	−14 43 15.02	21.02 ± 0.03	20.31 ± 0.05	0.29 ± 0.13	23000^{+9000}_{-5000}	LB-f1-548
BE_STIS_18	19 44 51.747	−14 43 13.87	21.08 ± 0.03	20.68 ± 0.05	0.07 ± 0.02	14000 ± 1000	LB-f1-557
BE_STIS_19	19 44 51.799	−14 43 10.62	21.77 ± 0.05	21.24 ± 0.10	0.30 ± 0.15	18100^{+3900}_{-3100}	LB-f1-573
BE_STIS_20	19 44 51.806	−14 43 17.16	21.24 ± 0.04	20.59 ± 0.06	0.12 ± 0.11	15100^{+2900}_{-2100}	LB-f1-547
BE_STIS_21	19 44 51.813	−14 43 18.25	21.45 ± 0.04	20.73 ± 0.07	0.06 ± 0.08	15000^{+3000}_{-1000}	LB-f1-544
BE_STIS_22	19 44 51.821	−14 43 07.57	16.82 ± 0.00	16.52 ± 0.01	0.51 ± 0.01	38300 ± 800	LB-f1-584
BE_STIS_23	19 44 51.864	−14 43 15.50	19.57 ± 0.02	18.82 ± 0.02	0.26 ± 0.05	23200^{+2800}_{-3200}	LB-f1-559
BE_STIS_24	19 44 51.872	−14 43 12.44	20.68 ± 0.03	20.07 ± 0.04	0.39 ± 0.10	25800^{+8200}_{-4800}	LB-f1-571
BE_STIS_25	19 44 51.894	−14 43 20.21	20.84 ± 0.03	20.08 ± 0.04	0.48 ± 0.03	45000^{+5000}_{-12000}	LB-f1-541
BE_STIS_26	19 44 51.894	−14 43 19.68	22.20 ± 0.06	21.46 ± 0.10	0.46 ± 0.06	38600^{+11400}_{-11600}	LB-f1-543
BE_STIS_27	19 44 51.938	−14 43 19.86	19.79 ± 0.02	19.05 ± 0.02	0.42 ± 0.04	35000^{+15000}_{-4000}	LB-f1-545
BE_STIS_28	19 44 51.989	−14 43 14.81	17.88 ± 0.01	17.23 ± 0.01	0.41 ± 0.01	38700^{+1300}_{-1200}	LB-f1-569
BE_STIS_29	19 44 52.011	−14 43 05.20	17.24 ± 0.01	16.73 ± 0.01	0.43 ± 0.01	38400 ± 900	LB-f1-597
BE_STIS_30	19 44 52.018	−14 43 17.91	20.79 ± 0.03	20.13 ± 0.04	0.18 ± 0.09	17000^{+3000}_{-2000}	LB-f1-561
BE_STIS_31	19 44 52.055	−14 43 17.83	21.26 ± 0.04	20.63 ± 0.06	0.49 ± 0.07	28000^{+5000}_{-7000}	LB-f1-563
BE_STIS_32	19 44 52.055	−14 43 14.87	17.00 ± 0.01	16.34 ± 0.01	0.41 ± 0.01	38300 ± 800	LB-f1-575
BE_STIS_33	19 44 52.062	−14 43 14.20	21.55 ± 0.05	21.10 ± 0.11	0.24 ± 0.15	15100^{+2900}_{-2100}	LB-f1-579
BE_STIS_34	19 44 52.062	−14 43 02.12	17.99 ± 0.01	17.49 ± 0.01	...	...	...
BE_STIS_35	19 44 52.070	−14 43 16.57	21.25 ± 0.04	20.53 ± 0.05	0.47 ± 0.05	38200^{+11800}_{-16200}	LB-f1-567
BE_STIS_36	19 44 52.091	−14 43 02.50	19.52 ± 0.02	19.23 ± 0.03	0.30 ± 0.01	18000 ± 1000	LB-f1-609
BE_STIS_37	19 44 52.128	−14 43 08.46	20.16 ± 0.02	19.45 ± 0.03	0.43 ± 0.05	34200^{+13300}_{-4200}	LB-f1-593
BE_STIS_38	19 44 52.187	−14 43 09.37	17.49 ± 0.01	16.79 ± 0.01	0.41 ± 0.01	40100 ± 100	LB-f1-594
BE_STIS_39	19 44 52.238	−14 43 18.27	20.30 ± 0.02	19.54 ± 0.03	0.24 ± 0.06	19900^{+4100}_{-1900}	LB-f1-574
BE_STIS_40	19 44 52.253	−14 43 12.37	22.39 ± 0.06	21.62 ± 0.14	0.14 ± 0.05	15600^{+2300}_{-700}	LB-f1-591
BE_STIS_41	19 44 52.282	−14 43 14.85	20.48 ± 0.03	19.75 ± 0.03	0.43 ± 0.03	38100^{+9400}_{-5100}	LB-f1-586
BE_STIS_42	19 44 52.304	−14 43 01.53	21.31 ± 0.04	21.32 ± 0.11	0.27:	16100:	LB-f1-621
BE_STIS_43	19 44 52.319	−14 43 16.19	20.91 ± 0.03	20.14 ± 0.05	0.45 ± 0.08	31800^{+18200}_{-8800}	LB-f1-585
BE_STIS_44	19 44 52.348	−14 43 15.88	17.82 ± 0.01	17.06 ± 0.01	0.40 ± 0.01	38300 ± 800	LB-f1-587
BE_STIS_45	19 44 52.370	−14 43 10.28	19.03 ± 0.01	18.28 ± 0.01	0.29 ± 0.01	23900^{+3100}_{-1900}	LB-f1-603
BE_STIS_46	19 44 52.384	−14 43 03.97	20.45 ± 0.02	20.54 ± 0.06	0.53 ± 0.08	24100^{+3900}_{-3100}	LB-f1-618
BE_STIS_47	19 44 52.399	−14 43 12.80	22.27 ± 0.06	21.43 ± 0.11	0.46 ± 0.17	26300^{+16200}_{-10300}	LB-f1-596
BE_STIS_48	19 44 52.399	−14 43 12.24	20.33 ± 0.02	19.64 ± 0.03	0.28 ± 0.09	20900^{+4100}_{-2900}	LB-f1-598
BE_STIS_49	19 44 52.406	−14 43 15.61	20.00 ± 0.02	19.26 ± 0.03	0.43 ± 0.05	35100^{+7400}_{-10100}	LB-f1-589
BE_STIS_50	19 44 52.414	−14 43 11.82	22.12 ± 0.05	21.47 ± 0.12	:	:	LB-f1-601
BE_STIS_51	19 44 52.487	−14 43 14.25	21.85 ± 0.05	21.33 ± 0.11	...	...	...
BE_STIS_52	19 44 52.502	−14 43 13.96	21.30 ± 0.04	20.60 ± 0.06	0.17 ± 0.12	17000^{+3000}_{-2000}	LB-f1-599
BE_STIS_53	19 44 52.502	−14 43 13.38	20.25 ± 0.02	19.60 ± 0.03	0.25 ± 0.06	20100^{+2900}_{-3100}	LB-f1-602
BE_STIS_54	19 44 52.516	−14 43 12.47	21.84 ± 0.05	21.29 ± 0.10	0.55 ± 0.12	31200^{+18800}_{-11200}	LB-f1-604
BE_STIS_55	19 44 52.648	−14 43 12.07	21.83 ± 0.05	21.48 ± 0.11	...	...	...
BE_STIS_56	19 44 52.670	−14 43 11.65	18.51 ± 0.01	17.76 ± 0.01	0.40 ± 0.01	37900 ± 400	LB-f1-610
BE_STIS_57	19 44 52.721	−14 43 21.44	22.12 ± 0.05	21.46 ± 0.11	...	...	...
BE_STIS_58	19 44 52.765	−14 43 12.02	18.24 ± 0.01	18.34 ± 0.01	0.63:	39500:	LB-f1-614
BE_STIS_59	19 44 52.824	−14 43 20.67	21.88 ± 0.05	21.24 ± 0.10	0.40 ± 0.15	21800^{+6200}_{-4800}	LB-f1-595
BE_STIS_60	19 44 52.831	−14 43 12.89	20.84 ± 0.03	20.23 ± 0.05	0.68:	50000:	LB-f1-616
BE_STIS_61	19 44 52.897	−14 43 11.38	21.14 ± 0.04	21.31 ± 0.13	0.45 ± 0.31	18100^{+5900}_{-5100}	LB-f1-626
BE_STIS_62	19 44 52.904	−14 43 12.20	17.08 ± 0.00	16.72 ± 0.01	0.50 ± 0.01	37900^{+2100}_{-400}	LB-f1-622
BE_STIS_63	19 44 52.904	−14 43 09.81	22.06 ± 0.05	21.71 ± 0.14	0.57 ± 0.25	22100^{+10900}_{-9100}	LB-f1-635
BE_STIS_64	19 44 52.926	−14 43 13.35	22.07 ± 0.07	21.75 ± 0.16	:	:	LB-f1-619
BE_STIS_65	19 44 52.934	−14 43 11.80	20.06 ± 0.02	19.91 ± 0.05	0.47 ± 0.15	22100^{+6900}_{-4100}	LB-f1-628

TABLE 4—*Continued*

Name	R.A. (J2000.0)	Decl. (J2000.0)	NUV	FUV	$E(B-V)$	$T_{\rm eff}$ (K)	ID[a]
BE_STIS_66	19 44 52.948	−14 43 12.38	22.07 ± 0.09	21.99 ± 0.28	...	...	...
BE_STIS_67	19 44 52.956	−14 43 11.03	20.45 ± 0.03	20.29 ± 0.05	0.65 ± 0.06	38200^{+11800}_{-18200}	LB-f1-632
BE_STIS_68	19 44 52.963	−14 43 12.35	19.56 ± 0.02	19.04 ± 0.02	0.58 ± 0.02	38300^{+4200}_{-3300}	LB-f1-627
BE_STIS_69	19 44 52.963	−14 43 11.70	20.07 ± 0.02	19.62 ± 0.04	0.61 ± 0.02	40200^{+4800}_{-2700}	LB-f1-630
BE_STIS_70	19 44 52.978	−14 43 13.41	21.02 ± 0.04	20.52 ± 0.06	...	...	...
BE_STIS_71	19 44 52.978	−14 43 11.67	19.79 ± 0.02	19.37 ± 0.03	...	...	...
BE_STIS_72	19 44 52.985	−14 43 11.16	19.65 ± 0.02	19.55 ± 0.03	0.62 ± 0.03	40800^{+9200}_{-6800}	LB-f1-636
BE_STIS_73	19 44 53.000	−14 43 12.75	18.23 ± 0.01	17.62 ± 0.01	0.47 ± 0.02	37000^{+5500}_{-3000}	LB-f1-629
BE_STIS_74	19 44 53.022	−14 43 12.17	20.19 ± 0.02	19.92 ± 0.04	0.73 ± 0.06	45100^{+4900}_{-16100}	LB-f1-634
BE_STIS_75	19 44 53.029	−14 43 11.34	20.43 ± 0.03	20.32 ± 0.05	0.70 ± 0.04	43100^{+6900}_{-14100}	LB-f1-640
BE_STIS_76	19 44 53.044	−14 43 12.07	21.11 ± 0.04	21.23 ± 0.12	0.76 ± 0.03	40000^{+10000}_{-6000}	LB-f1-637
BE_STIS_77	19 44 53.073	−14 43 11.26	19.86 ± 0.02	19.73 ± 0.03	0.64 ± 0.04	37000^{+13000}_{-5000}	LB-f1-644
BE_STIS_78	19 44 53.175	−14 43 12.92	20.16 ± 0.02	19.80 ± 0.04	0.53 ± 0.02	35100^{+7400}_{-2100}	LB-f1-646
BE_STIS_79	19 44 53.183	−14 43 12.48	21.16 ± 0.03	20.74 ± 0.07	0.43 ± 0.10	22000 ± 10000	LB-f1-648
BE_STIS_80	19 44 53.219	−14 43 12.29	21.52 ± 0.04	21.12 ± 0.11	0.44 ± 0.16	21200^{+6800}_{-5200}	LB-f1-651

NOTES.—Units of right ascension are hours, minutes, and seconds, and units of declination are degrees, arcminutes, and arcseconds. A lone colon indicates an unknown value, and a colon after a value indicates uncertainty. Table 4 is also available in the electronic edition of the *Astronomical Journal*.

[a] The last column provides the cross-identification with the WFPC2 photometric study by Bianchi et al. (2001b). Magnitudes are in the VEGAMAG system.

sources from Bianchi et al. (2001b), are listed in Table 4. The coordinates are from the STIS images; however, we applied a constant shift of +0.″684 and −0.″54 in right ascension and −0.″684 and −0.″72 in declination for fields o66410 and o66420, respectively, in order to register the astrometry to the WFPC2 coordinates of Bianchi et al. (2001b). After the shift, positions for matched stars coincided within 0.″2.

4. RESULTS AND DISCUSSION

Absolute magnitudes for our sample were calculated using the reddening derived in § 3 and a distance modulus of DM = 23.47 (McGonegal et al. 1983). In Figure 9 the color-magnitude diagram for stars in the group 1 fields is shown with superposed theoretical isochrones for $Z = 0.004$ from Girardi et al. (2002) and Bertelli et al. (1994). Isochrones for solar metallicity do not fit the observations as well. The majority of the group 1 stars with five-band photometry (34 stars, or 74%) are in the association OB 15 (Hodge 1977) centered at R.A. = $19^{\rm h}45^{\rm m}14^{\rm s}$, decl. = $-14^{\circ}45'7''$, with an angular size of ≈90″ (≈200 pc linear size) and a distance from the center of the galaxy of ≈5′, or 730 pc. The main part of the association is included in the WF3 chip of field 36 shown in Figure 5. For these stars we estimated $T_{\rm eff} >$ 20,000 K (spectral type earlier than B2). Their "scale distance," defined as the largest distance between two close neighbors in the group (see Battinelli 1991; Ivanov 1996), is $d_S = 26''$ (46 pc), and the mean distance between close neighbors is $d_M = 5''$ (13 pc), with $\sigma = 4.''5$ (11.4 pc). If we add fainter hot star candidates that have photometry only in three bands, using the $(m_{336} - m_{439})_0 < -1$ and $(m_{439} - m_{555})_0 < 0.0$ criteria to select stars hotter than 16,000 K (i.e., earlier than spectral type ∼B5 V), we find 35 additional stars in OB 15 (down to magnitude $V_0 = 22.2$ [$V \approx 23.0, M_V = -1.27$]), and the association properties become $d_S = 13''$ (32 pc) and $d_M = 4''$ (10 pc) with $\sigma = 3''$ (8 pc). The total number of stars with estimated $T_{\rm eff} > 16{,}000$ K in OB 15 is therefore about 70. The expected foreground contamination is negligible for the hot star sample (§ 3.1), so we assume all of the observed massive stars to be members of the OB association. The H-R diagram indicates the stellar population in OB 15 to be younger than 10 Myr.

Our data, geared toward the characterization of the young massive stars, do not provide conclusive information on the number of red supergiants. In fact, the *U*-band filter drives the magnitude limit in our restricted sample to very bright limits for cool stars [$m_{555} \approx 20.5$, or $(m_{555})_0 = 19.7$ and 19.3 in OB 8 and OB 15, respectively]. If we consider the $(B - V)$ color only, we can reach fainter magnitudes (see Fig. 4), but we have no way to separate the foreground (MW halo) dwarfs from the NGC 6822 supergiants, whose apparent magnitudes are in the same range (e.g., Massey 1998b; Bianchi et al. 2001a). The number of red foreground stars [$(B - V) > 1.3$] expected from the model of Ratnatunga & Bahcall (1985) is 0.35 arcmin^{-2} down to $V = 19$ and

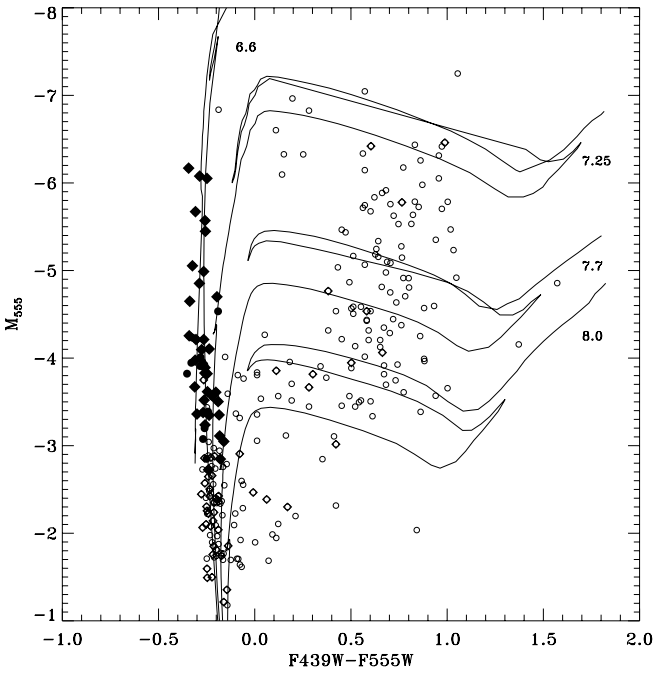

FIG. 9.—H-R diagram for the stars in the group 1 fields (wider sample). The observed magnitudes and colors have been dereddened as described in § 3. The filled symbols represent the stars with good photometry in all five filters used. Stars in the region of the OB 15 association are shown as diamonds, and stars outside this region as circles. Isochrones for $Z = 0.004$ from Girardi et al. (2002) and Bertelli et al. (1994) are shown, with ages (in logarithmic years) indicated.

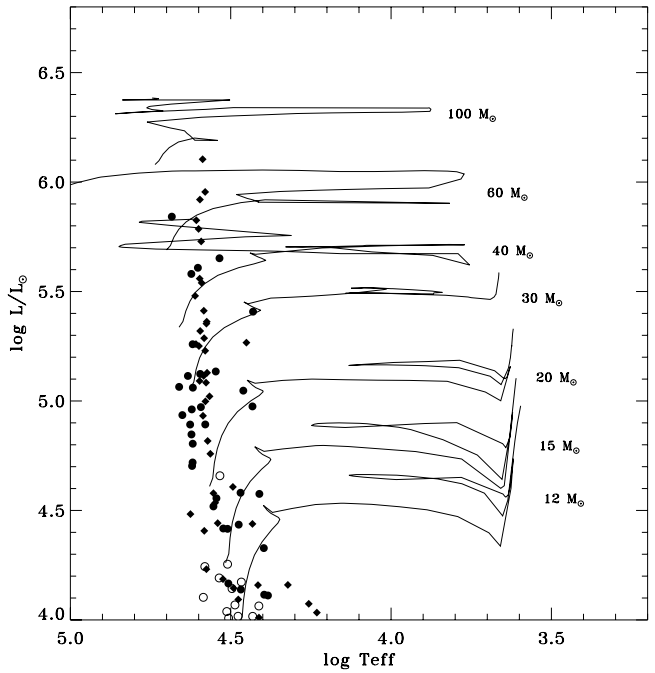

FIG. 10.—H-R diagram of the hot stars in the area of the OB 15 association (filled circles show stars with five-band photometry, and open circles show stars with U, B, and V only) and in the OB 8 field (*diamonds*). Overplotted are the evolutionary tracks of Fagotto et al. (1994) for $Z = 0.004$. Redder stars with the same range of luminosity are not shown because the foreground contamination is significant.

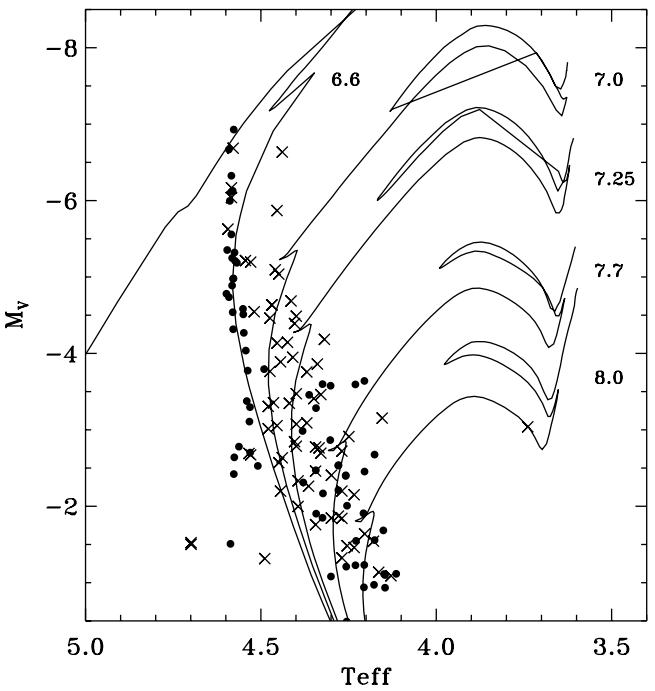

FIG. 11.—H-R diagram of the Hubble V region. The results from combined STIS (this paper) and WFPC2 (Bianchi et al. 2001b) photometry are shown with filled circles. For comparison, the results from Bianchi et al. (2001b) are also plotted (*crosses*). Isochrones for $Z = 0.004$ from Girardi et al. (2002) and Bertelli et al. (1994) are plotted, and ages (in logarithmic years) are indicated.

1.5 arcmin^{-2} between $V = 19$ and 21. Therefore, we expect 24 and 35 red foreground stars brighter than $V = 21$ in our group 2 and group 1 samples, respectively. The number of stars with measured photometry $(B - V) > 1.3$, $V < 21$ is 14 and 32, respectively, in the group 2 and group 1 samples. Considering the effects of small-number statistics, no detection of red supergiants can be claimed without spectroscopic follow-up, which we plan to pursue. A better estimate of the evolved stellar population in this region can be obtained from the red supergiant survey of Massey (1998b). This survey is complete (photometrically) to $V = 20.5$. The OB 15 association is contained in Massey's N6822-C field. There is only one star (NGC 6822C-438) from the Massey (1998b) catalog inside the OB 15 area, and it is classified by the author as a foreground object. The four closest neighbors are also classified as foreground stars, so we can conclude that there are no red supergiants in the region of OB 15 and that we are looking at stars born in a very recent star formation process in that field. The nondetection is consistent with the expected number from evolutionary models. In the initial mass range in which both blue and red supergiants are expected to coexist in the H-R diagram, 15–30 $M_\odot$ (e.g., Salasnich et al. 1999), our sample is complete only for the blue objects. At the higher end of this mass range, even if all of our blue stars were supergiants, we would expect less than one red supergiant in the sample (although the ratio depends on metallicity and rotation; extremely high rotation can reverse the ratio; see Maeder & Meynet 2001).

The physical H-R diagram for the associations OB 15 and OB 8 is shown in Figure 10 with the evolutionary tracks of Fagotto et al. (1994) for $Z = 0.004$. The initial mass value is indicated for each track. The lower mass limit ($\approx 12\ M_\odot$) reflects the depth of our photometry for stars with five-band measurements: the magnitude limit is $m_{555} = 21.5$, which for an average $E(B - V) = 0.27$ and DM = 23.47 corresponds to $M_V = -2.7$ or spectral type $\sim$B2 V. A few very massive star candidates are found. The errors on photometrically derived luminosity and mass are unavoidably large and will be refined with follow-up spectroscopy. The most massive star in OB 15, taking into account the uncertainties in temperature and luminosity, can be placed within a range of masses between 40 and 70 $M_\odot$. The range is slightly higher for OB 8. For the objects with good photometry in all five bands the uncertainties in the photometrically derived $T_{\rm eff}$ are typically $\sim$20%. To refine the stellar parameters and to determine more precisely the mass distribution, a spectroscopic study needs to be done. The UV bands F170W and F255W used in this study give us an opportunity to distinguish between the optically brightest (M_V) and the bolometrically most luminous stars with highest effective temperatures and largest bolometric corrections.

The association OB 8 contained in our STIS observations is much more compact (size about 35″ or 85 pc, of which $25'' \times 25''$ or 60 pc $\times$ 60 pc is covered by the STIS image) and densely populated. We detect 80 stars in our STIS FUV and NUV imaging ($25'' \times 25''$) of this region, down to a limit of $m_{\rm NUV} = 22.5$ ($V \approx 23.4$), and derive physical parameters for 72 of them that are also contained in the WFPC2 photometric sample of Bianchi et al. (2001b). The mean distance between closest neighbors is $d_M = 1''.2$ (3 pc), and the maximum separation (scale distance) is $d_S = 7''.5$ (18 pc). There is an H II region associated with this object, Hubble V. Its nebular properties were studied by O'Dell et al. (1999), and its young stellar population by Bianchi et al. (2001b). The H-R diagram derived from our STIS photometry is shown in Figure 11, together with the previous results from Bianchi et al. (2001b). The temperatures estimated for most stars in this sample are $T_{\rm eff} > 15{,}000$ K, consistent with spectral classes earlier than $\sim$B5 V. The extinction is higher in this region, having a mean value $E(B - V) \sim 0.4$, with large variations.

The values of $E(B - V)$ found in our WFPC2 fields suggest that in regions far from the galaxy center the reddening is mostly

MW foreground dust. The average value for all the stars in the group 1 fields is $E(B-V) = 0.27$, with a standard deviation of 0.14. For the hot star sample the mean value of the reddening obtained by χ^2 fitting is $E(B-V) = 0.29$, with $\sigma = 0.06$. The stars in the group 2 fields show a similar distribution of reddening, with a mean value of $E(B-V) = 0.22$ and standard deviation of 0.12. The large scatter and somewhat lower value than the average extinction toward NGC 6822 are likely due to the fact that most stars detected in this field are foreground MW stars.

5. CONCLUSIONS

We have explored with *HST* multiband imaging four extremely different environments in NGC 6822. In the group 2 fields, ≈1.5–2.0 kpc off (north of) the galaxy center, we find a very small number of hot stars, comparable to the expected number of foreground stars. The entire sample in the group 2 fields is dominated by foreground stars, at least down to $V \sim 22$, and consistently, we find in this area the smallest extinction [average $E(B-V) = 0.22$] measured in this galaxy. At fainter magnitudes, we find up to ∼7 times more stars than the Ratnatunga & Bahcall (1985) model for MW stars predicts. However, these authors warn that their extrapolation to faint magnitudes is uncertain, so our fainter objects may be either stars in the outskirts of NGC 6822 or foreground stars that the current MW model fails to predict. The group 1 fields, covering an area of 19 arcmin^2 (≈402 kpc^2) east of the galaxy's main bar, include the OB 15 association (≈90″, or 200 pc size). In OB 15 there are 34 (out of the 46 total in the group 1 sample) hot massive stars hotter than ∼20,000 K (in our restricted sample photometry with limit $V \approx 21.5$, corresponding to a ∼B2 V star at the distance of NGC 6822). About 35 additional stars (detected in U, B, and V only) have an estimated $T_{\rm eff} > 16{,}000$ K. The H-R diagram indicates an age of a few million years for OB 15. The general field population, in the group 1 fields excluding OB 15, contains much fewer hot massive stars. We found 25 A-type supergiant candidates in the group 1 fields outside of OB 15. These objects are visually bright and would be ideal targets for ground-based spectroscopy to determine chemical abundances.

The fourth environment, studied with STIS imaging, covers a much smaller and more crowded area, including most of the OB 8 association in the H II region Hubble V, whose nebular properties and stellar content were previously studied by O'Dell et al. (1999) and Bianchi et al. (2001b), respectively. Our new STIS imaging provides a gain of ≈2 mag in NUV over our previous study (Bianchi et al. 2001b), and the first FUV imaging, as well as the best resolution (0.06 pc pixel^{-1}), of this compact cluster. In this $25'' \times 25''$ (60 pc × 60 pc) field, we measure 80 stars in both NUV and FUV, down to magnitude 22.5 in NUV ($V_0 \approx 22.2$, ≈B5 V).

To compare the general properties of the young stellar populations in OB 15 and OB 8, we estimate the average density of hot stars per unit area down to the magnitude limit of $V_0 = 22.2$ or $M_V = -1.27$ (approximately spectral type B5 V). We find a density of 40 and 460 hot stars arcmin^{-2}, i.e., 0.0019 and 0.0218 stars pc^{-2}, in OB 15 and OB 8, respectively, adopting sizes of 80″ and 25″ for OB 15 and OB 8. In the general field (group 1) the density of hot stars detected is much lower, 0.7 arcmin^{-2} (3×10^{-5} pc^{-2}). Assuming that the IMF does not vary, and given the similar ages of these two associations as indicated by their H-R diagrams, the ratio of hot star density above the same intrinsic magnitude limit should correspond directly to the ratio of star formation *density* among the two regions. Therefore, the star formation surface density is higher in OB 8 than in OB 15 by a factor of 12, while the total star formation rate is the same in both associations (approximately 70 stars hotter than 16,000 K). We scaled the total number of stars with $M > 12\ M_\odot$ according to their absolute luminosity (42 and 44 stars) to derive the total mass of the clusters. Assuming a Salpeter IMF ($\alpha = 2.35$) over a mass range of 100–1 $M_\odot$ (for comparison to other works on Local Group galaxies), we estimate a cluster mass of $M_{\rm tot} \sim (3.5-4) \times 10^3\ M_\odot$. By using instead IMF $= AM^{-\alpha}$ with $\alpha = 2.3$ in the range 0.5–100 $M_\odot$ and $\alpha = 1.3$ in the range 0.1–0.5 $M_\odot$ (Kroupa 2001) we estimate a total mass of the clusters of $M_{\rm tot} \sim (6-7) \times 10^3\ M_\odot$ in the wider mass range of 0.1–100 $M_\odot$.

This result is interesting in view of the numerous current studies estimating the star formation in more distant galaxies, or in nearby extended galaxies with lower resolution imaging (e.g., Calzetti et al. 2005; Bianchi et al. 2005; Thilker et al. 2005; and references therein). In the case of the two star-forming regions studied, integrated measurements such as UV or IR emission might estimate the total star formation to be equal but not discern the extremely differing spatial properties. The Hα emission, another indicator of star formation, also reflects the different spatial properties of the associations. We measured the Hα emission in the regions of Hubble V and OB 15 using publicly released images from the recent NOAO survey of the Local Group (Massey et al. 2006) and examined the Hα morphology. The Hα flux, when integrated over the spatial extent of the stellar associations, is about 3 times higher in Hubble V than in OB 15. However, while the Hα emission in Hubble V appears compact, as is the stellar cluster, the OB 15 association is surrounded by a larger, multishell-like Hα envelope. When we integrate the Hα flux over this larger bubble, seemingly associated with the OB 15 stars from its morphology, its total flux is comparable to the emission from Hubble V. It is also important that we could extend the census of massive stars in these two associations down to early B spectral types, for which a few megayears age difference would not change the sample (numerical) statistics, making the comparison robust. Earlier ground-based surveys comparing the massive star content of Local Group galaxies were necessarily limited to higher masses, at which both small-number (IMF) statistics and a few megayears difference in the ages of the very young clusters (dominating the census of massive stars) can bias the results significantly. For example, the Massey et al. (1995) seminal paper on three representative Local Group galaxies M31, M33, and NGC 6822 compared the number of stars more massive than 40 $M_\odot$ per kpc^2. From the massive star content, we estimated the total mass of the associations and found $\sim 4 \times 10^3\ M_\odot$ for a mass range of 1–100 $M_\odot$ (Salpeter IMF), or $\sim 7 \times 10^3\ M_\odot$ extending the mass range to 0.1 $M_\odot$ with the IMF of Kroupa (2001).

Our results confirm and quantify previous evidence that the recent/current star formation in NGC 6822 occurs episodically with extreme spatial variations in intensity and modality. The earlier star formation in this galaxy, according to Gallart et al. (1996b) and Wyder (2003), has proceeded smoothly (relatively constant, or slightly increasing with time) until ≈1 Gyr ago. Of course, while time and space variations of the recent star formation can be appreciated in detail from the study of young massive stars, such distinctions cannot be made for older populations, for which the star formation history is inferred from an H-R diagram integrated over longer epochs, and dynamical relaxation blurs or erases initial spatial structures. More extended imaging studies of the entire galaxy are planned using *GALEX* (far-UV and near-UV) and ground-based imaging. Follow-up detailed studies of the stellar properties are planned with ground-based (Very Large Telescope) spectroscopy.

We thank the referee for insightful comments and J. Maiz for assistance with installation and use of the CHORIZOS code. This work is based on data from the *Hubble Space Telescope*. Support for program GO-8675 was provided by NASA through a grant from the Space Telescope Science Institute, which is operated by the Association of Universities for Research in Astronomy, Inc., under NASA contract NAS5-26555. The work was also partly supported by NASA grant NAG5-9219 (NRA-99-01-LTSA-029).

REFERENCES

Battinelli, P. 1991, A&A, 244, 69
Bertelli, G., Bressan, A., Chiosi, C., Fagotto, F., & Nasi, E. 1994, A&AS, 106, 275
Bertin, E., & Arnouts, S. 1996, A&AS, 117, 393
Bianchi, L., Catanzaro, G., Scuderi, S., & Hutchings, J. B. 2001a, PASP, 113, 697
Bianchi, L., Scuderi, S., Massey, P., & Romaniello, M. 2001b, AJ, 121, 2020
Bianchi, L., et al. 2005, ApJ, 619, L71
Calzetti, D., et al. 2005, ApJ, 633, 871
Dolphin, A. 2000, PASP, 112, 1397
Fagotto, F., Bressan, A., Bertelli, G., & Chiosi, C. 1994, A&AS, 105, 29
Gallart, C., Aparicio, A., Bertelli, G., & Chiosi, C. 1996a, AJ, 112, 1950
———. 1996b, AJ, 112, 2596
Girardi, L., Bertelli, G., Bressan, A., Chiosi, C., Groenewegen, M. A. T., Marigo, P., Salasnich, B., & Weiss, A. 2002, A&A, 391, 195
Hodge, P. W. 1977, ApJS, 33, 69
Holtzman, J. A., Burrows, C. J., Casertano, S., Hester, J. J., Trauger, J. T., Watson, A. M., & Worthey, G. 1995a, PASP, 107, 1065
Holtzman, J. A., et al. 1995b, PASP, 107, 156
Hubble, E. P. 1925, ApJ, 62, 409
Hutchings, J. B., Cavanagh, B., & Bianchi, L. 1999, PASP, 111, 559
Ivanov, G. R. 1996, A&A, 305, 708
Kayser, S. E. 1967, AJ, 72, 134
Kroupa, P. 2001, MNRAS, 322, 231
Kurucz, R. L. 1993, in IAU Colloq. 138, Peculiar versus Normal Phenomena in A-Type and Related Stars, ed. M. M. Dworetsky, F. Castelli, & R. Faraggiana (ASP Conf. Ser. 44; San Francisco: ASP), 87
Lejeune, T., Cuisinier, F., & Buser, R. 1997, A&AS, 125, 229
Maeder, A., & Meynet, G. 2001, A&A, 373, 555
Maíz-Apellaniz, J. 2004, PASP, 116, 859
Massey, P. 1998a, in Stellar Astrophysics for the Local Group, ed. A. Aparicio, A. Herrero, & F. Sanchez (Cambridge: Cambridge Univ. Press), 95
———. 1998b, ApJ, 501, 153
Massey, P., Armandroff, T. E., Pyke, R., Patel, K., & Wilson, C. D. 1995, AJ, 110, 2715
Massey, P., Olsen, K. A. G., Hodge, P. W., Strong, S. B., Jacoby, G. H., Schlingman, W., & Smith, R. C. 2006, AJ, 131, 2478
McGonegal, R., McLaren, R. A., Welch, D. L., Madore, B. F., & McAlary, C. W. 1983, ApJ, 273, 539
McMaster, M., & Whitmore, B. 2002, in *HST* Calibration Workshop ed. S. Arribas, A. Koekemoer, & B. Whitmore (Baltimore: STScI), 350
O'Dell, C. R., Hodge, P. W., & Kennicutt, R. C., Jr. 1999, PASP, 111, 1382
Ratnatunga, K. U., & Bahcall, J. N. 1985, ApJS, 59, 63
Romaniello, M. 1998, Ph.D. thesis, Univ. Pisa
Salasnich, B., Bressan, A., & Chiosi, C. 1999, A&A, 342, 131
Thilker, D., et al. 2005, ApJ, 619, L79
Wyder, T. K. 2003, AJ, 125, 3097